Materials and Interfaces

Review

CO-Resistant Surface Dopant Engineering of Pt/Pd Catalysts for High-Performance Liquid Fuel Oxidation Reactions

Mrinal Kanti Kabiraz [†], Joyjit Kundu [†], Shajahan Shaik, and Sang-Il Choi *

Department of Chemistry and Green-Nano Materials Research Center, Kyungpook National University,
Daegu 41566, Republic of Korea
* Correspondence: sichoi@knu.ac.kr
† These authors contributed equally to this work.

Received: 10 October 2025; Revised: 20 November 2025; Accepted: 25 November 2025; Published: 23 December 2025

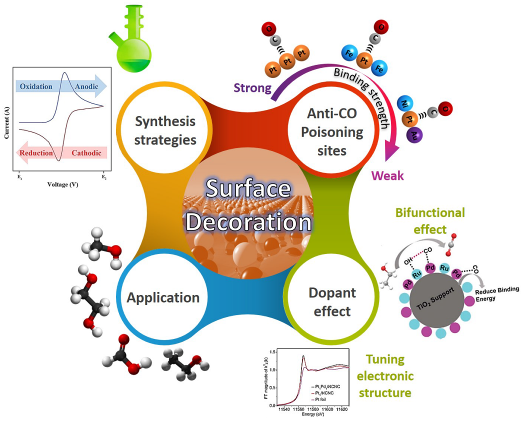

Abstract: Surface dopant engineering has emerged as a powerful approach to enhance the catalytic properties of Pt and Pd nanomaterials by introducing site-specific modifications at the atomic scale. In liquid fuel oxidation reactions (LFORs), surface-decorated Pt/Pd catalysts demonstrate remarkable activity and durability by providing engineered sites that mitigate the long-standing challenge of carbon monoxide (CO) poisoning. Transition metal atoms and their oxides anchored on Pt/Pd surfaces act as anti-CO centers, facilitating more efficient fuel oxidation pathways while preserving catalytic stability. This review highlights recent advances in surface-decorated Pt/Pd catalysts, emphasizing the underlying mechanisms of CO resistance, synthetic strategies for dopant incorporation, and the structure-performance correlations that define their electrocatalytic behavior. We also summarize the performances achieved in methanol, ethanol, and other liquid fuel oxidation systems using dopant-engineered catalysts. Finally, we discuss the remaining challenges and future opportunities in rationally designing CO-tolerant catalytic surfaces for next-generation energy conversion devices.

Keywords: surface dopant engineering; platinum; CO poisoning; fuel cell; electrocatalysis

1. Introduction

Renewable energy technology can tackle the current global energy crisis while minimizing environmental pollution. As a renewable energy technology, a direct liquid fuel cell (DLFC) has been regarded as one of the promising energy conversion devices that can convert the chemical energy of liquid fuels such as methanol, ethanol, and formic acid into electrical energy [1–4]. This DLFC system has certain advantages compared to hydrogen (H_2)-based fuel cells: low cost, plentiful, easy to transport, and safe to store. However, practical applications of DLFCs are limited mainly due to the poisoning effect of a reaction intermediate, such as carbon monoxide (CO), on the surface of catalysts, resulting in sluggish kinetics of anodic liquid fuel oxidation reaction (LFOR) and thus deteriorating the cell performances [5–7]. For example, platinum (Pt) and palladium (Pd) have been utilized as excellent LFOR catalysts, but their LFOR performances rapidly decrease owing to the CO adsorption (CO_{ads}) on their surfaces [8–12]. Therefore, from the viewpoint of catalyst poisoning, one way to improve LFOR is to develop state-of-the-art catalysts with anti-CO-poisoning sites [13–17]. Interestingly, decorating the surface of Pt/Pd catalysts with transition metal dopants, including Ru, Sn, Pd, Ni, and Cu, has been reported to create favorable surface-active sites toward LFOR. It is well-known that these dopants could increase the catalytic surface roughness, resulting in the non-continuous distribution of CO and thus the tolerance of the strong CO_{ads} behavior [18–20]. In addition, metal dopants on the surface of Pt/Pd promote the water dissociation at a lower potential, and the adsorbed OH (OH_{ads}) facilitates the oxidation of CO_{ads} to CO_2 [21–24]. These attractive features of surface metal dopants have drawn much attention from the research community. Although there have been numerous articles related to the metal dopant strategy, to the best of our knowledge, there is an absence of a comprehensive overview of decorating anti-CO poisoning metal dopants on the surface of Pt/Pd nanocrystals for LFOR. Therefore, in this review, we discuss the underlying LFOR mechanisms in pristine and decorated catalyst surfaces, the metal doping synthesis strategies, advanced techniques to analyze LFOR, and the electrocatalytic performances of various LFOR. The liquid fuels discussed in this review are limited to ethanol, methanol, formic acid, and ethylene glycol (EG), considering their close feasibility in the practical DLFC systems regarding chemical energy density per volume and efficiency (Table 1). It is evident that liquid fuels, despite their higher theoretical chemical energy density per unit volume compared to H_2, still encounter significant challenges in DLFCs. The primary concern with DLFCs is the catalyst poisoning caused by CO. As such, in this review, we place emphasis on dopant metals as bifunctional catalytic sites and attribute them as anti-CO poisoning agents to tackle this issue. Finally, we outline the future designs of selective and highly stable electrocatalysts toward LFOR and provide practical insights for the DLFC applications.

Table 1. The number of electrons transferred, theoretical energy density normalized with fuel weight (W_s) and volume (W_e), standard redox potential, and theoretical energy conversion efficiency for various liquid fuels [25–27].

Liquid Fuel	Number of Electrons Transferred	W_s (kWh·kg^{-1})	W_e (kWh·l^{-1})	Standard Redox Potential (V)	Efficiency (%)
Hydrogen	1	32.80	1800	1.23	83
Formic acid	2	2.08	2086	1.40	99
Methanol	6	4.69	4820	1.21	97
Ethanol	12	8.99	6280	1.15	63
Ethylene glycol	10	5.27	5800	1.22	99

2. Understanding of LFOR Mechanisms

A typical working process of a DLFC is illustrated in Figure 1a. Liquid fuel is fed directly to the anode of the DLFC, and air/oxygen gas is provided to the cathode for the oxygen reduction reaction (ORR). During the fuel cell operation, charged ions pass through the membrane, and the electrons travel via an external circuit, generating electricity. To boost the DLFC performance, understanding of CO_{ads} configuration on the catalyst surface at the anode is essential. At the anode, electrocatalytic reactions using Pt-/Pd-based catalysts are generally hampered by the presence of CO_{ads}, as illustrated in Figure 1b. CO_{ads} can exist in two distinct configurations, namely top-type and bridge-type. The CO_{ads} configuration can be determined by IR analysis, which reveals a decrease in vibrational frequencies, indicating a stronger interaction of CO [28]. It has been observed that removing bridge-type CO_{ads} from the catalytic surface is more difficult compared to top-type CO_{ads}, as evidenced by the decreased vibrational frequencies in Figure 1c. Therefore, oxidizing bridge-type CO_{ads} to CO_2 requires more energy, as depicted in Figure 1c. Additionally, bridge-type CO_{ads} tend to be more prevalent on continuous Pt/Pd atom arrangements. Therefore, increasing the surface roughness of the catalyst by adding transition metal dopants can generate catalytic sites favoring a top-type CO_{ads} and disrupt the formation of bridge-type CO_{ads} [29,30]. In addition, decorating transition metal dopants (M) on the surface of Pt/Pd assists the dissociation of water molecules at a lower overpotential compared to the pristine Pt/Pd surface, and the produced OH_{ads} adsorbs preferentially on the dopants (M–OH_{ads}) [31,32]. Then, the M–OH_{ads} facilitates the oxidation of CO_{ads} to CO_2 on the neighboring Pt sites ($Pt–CO_{ads} + M–OH_{ads} \rightarrow CO_2 + H^+ + e^- + Pt + M$) [33,34]. Therefore, a proper understanding of the reaction mechanism at a molecular level on the catalyst surface containing metal-dopants is important to enhance the performance of LFOR.

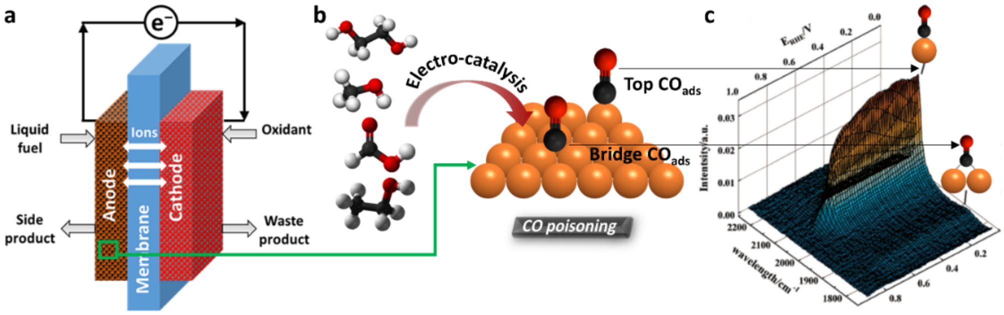

Figure 1. (**a**) A schematic illustration of a DLFC. (**b**) Indirect pathway during LFOR leading to catalyst poisoning by produced CO_{ads}. (**c**) Top and bridged CO_{ads} showing different IR spectra at different potentials. Reproduced with permission [28]. Copyright 2005, American Chemical Society.

2.1. Mechanism for Ethanol Oxidation Reaction (EOR)

Ethanol oxidation on Pt-/Pd-based catalysts generally proceeds through two competing pathways (Figure 2a) [35–37]. The direct pathway involves the complete oxidation of ethanol to CO_2, while the indirect pathway leads to incomplete oxidation to acetate anion. Both routes begin with the initial dehydrogenation of ethanol by breaking the C_α–H and O–H bonds [38], forming the stable $*CH_3CO$ intermediate (Figure 2a) [39]. In the direct pathway, the C_β-dehydrogenation of $*CH_3CO$ on pure Pt is the rate-determining step (RDS), producing intermediates such as $*CH_2CO$ and $*CHCO$. These are ultimately oxidized to $*CO_{ads}$, which must be removed by OH-assisted oxidation to generate CO_2 [38]. However, the strong binding of *CO on Pt/Pd surfaces often leads to poisoning, limiting the C_1 route. As a result, the reaction frequently diverts toward the C_2 pathway, where $*CH_3CO$ is oxidized to acetate without C–C bond cleavage [40].

For example, the DFT calculation of Pt(100) and Rh–O decorated Pt(100) surfaces provides direct evidence of their mechanistic differences during ethanol oxidation [41]. The calculated free energy profiles (Figure 2b,c) highlight the contrast clearly. On pure Pt(100) (Figure 2b), ethanol sequentially dehydrogenates to $*CH_3CO$, but the strong *CO adsorption and high barriers for its removal ($E_a \approx 0.92$–0.94 eV) restrict the direct pathway, causing poisoning and favoring C_2 product formation. By contrast, Rh–O decorated Pt(100) (Figure 2c) not only lowers the energy barrier for the potential-limiting step ($*CH_3CH_2OH \rightarrow *CH_3CHOH$, $\Delta G \approx 0.27$ eV) but also facilitates C–C scission of $*CH_3CO$. Importantly, Rh–O sites weaken *CO binding and accelerate its OH-assisted oxidation ($E_a = 0.72$ and 0.24 eV), ensuring rapid *CO turnover and enabling near-complete ethanol oxidation to CO_2 at relatively low potentials.

Beyond single-site decoration, additional metal dopants can further promote full ethanol oxidation (Figure 2d,e). Transition metals (M) incorporated into the Pt/Pd surface enhance water dissociation, generating M–OH_{ads} that accelerate *CO oxidation on adjacent Pt/Pd sites (Figure 2d) [42,43]. This bifunctional effect alleviates poisoning and sustains the direct C_1 route. Moreover, introducing a second dopant creates a synergistic trimetallic environment that stabilizes intermediates in favorable adsorption geometries. For instance, on a Pt–Rh–M surface, $*CH_3CO$ can adopt a chair-like configuration in which the C_α atom binds to Pt, the C_β atom strongly interacts with Rh, and the O atom coordinates with M (Figure 2e) [38]. This geometry lowers the barrier for C–C bond cleavage, making the pathway to CO_2 more accessible. Thus, multi-metallic decoration integrates bifunctional OH supply with geometric stabilization of intermediates, offering a powerful strategy to overcome CO poisoning and achieve complete EOR.

2.2. Mechanism for Methanol Oxidation Reaction (MOR)

Pt-/Pd-based catalysts have been reported to possess good activity and stability toward the MOR in acidic and alkaline media [44]. Previous studies indicated that electrocatalytic MOR performance is better in alkaline than in acidic media. In alkaline media, methanol and OH^- are initially adsorbed on the catalyst surface (Figure 3a). Subsequently, methanol dissociates into various CH_XO species and is continuously oxidized by OH_{ads}. The continuous supply of OH_{ads} comes from the water dissociation. In the final step, CO_{ads} react with OH_{ads} to generate CO_2 [45]. The MOR mechanism in acidic media differs from the alkaline one (Figure 3b). When the methanol is adsorbed on the Pt/Pd surface, the C–H bonds dissociate, leading to the formation of CO_{ads} intermediates and finally generation of CO_2 by reacting with OH_{ads}.

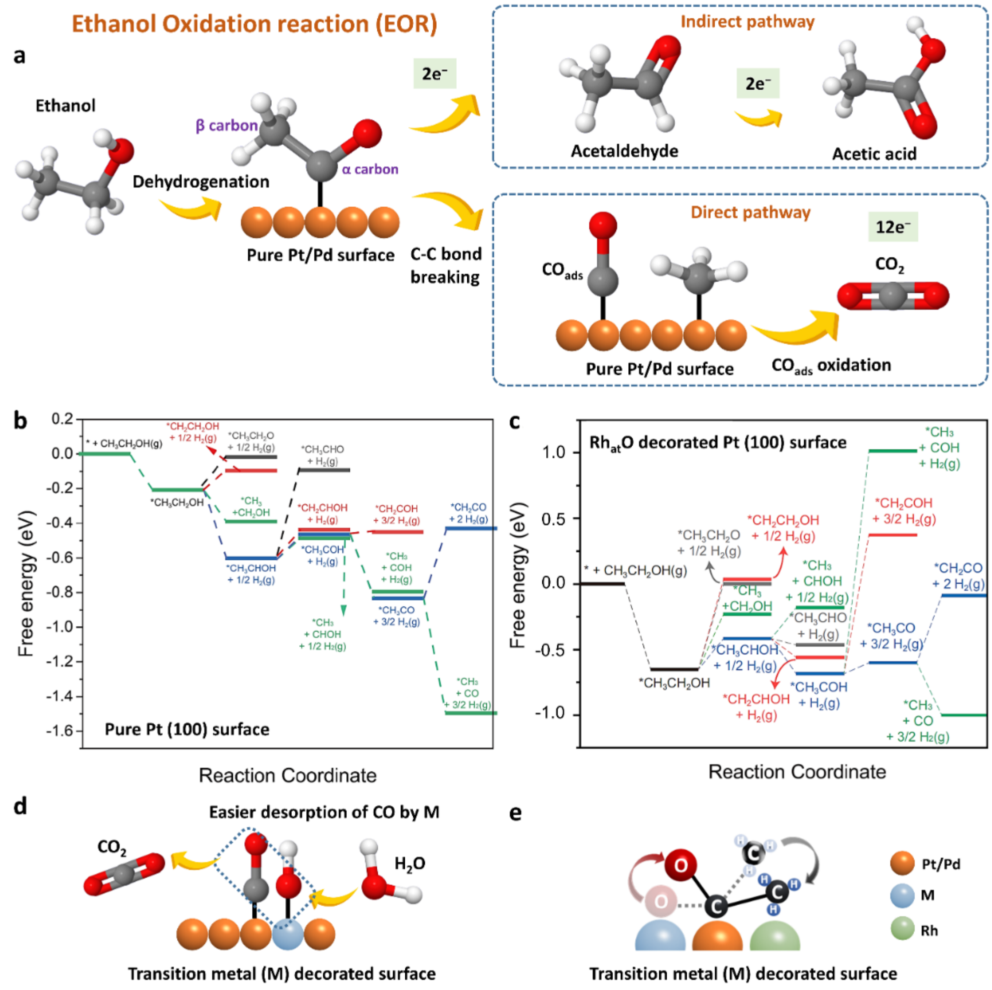

Figure 2. (**a**) Reaction pathways for the EOR mechanism on the pure Pt/Pd surface. (**b**) Free energy profile on Pt(100), where strong *CO adsorption limits C–C cleavage and favors C_2 products. (**c**) Free energy profile on Rh–O decorated Pt(100), where weakened *CO binding and faster CO oxidation promote complete oxidation to CO_2. Reproduced with permission [41]. Copyright 2022, National Academy of Sciences. (**d**) Bifunctional role of dopant atoms (M) in generating M–OH_{ads} that oxidize *CO_{ads} on neighboring Pt/Pd sites. (**e**) Chair-like adsorption of *CH_3CO on a trimetallic Pt–Rh–M surface, lowering the C–C cleavage barrier and driving full EOR.

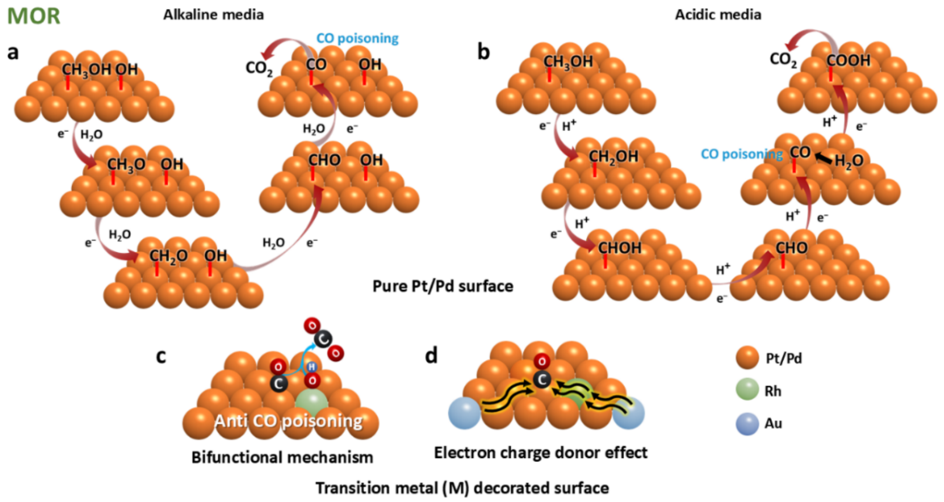

Figure 3. Reaction pathways for MOR in (**a**) alkaline and (**b**) acidic media on pure Pt/Pd surface. (**c**) Bifunctional mechanism of transition metal M decorated surface. (**d**) Stable adsorption configurations of CH_3CO* on M–Pt–Rh sites.

However, these MOR mechanisms are inhibited by strong CO_{ads} on the Pt/Pd surface, reducing the reaction between CO_{ads} and OH_{ads}. Therefore, introducing metal dopants that prefer OH_{ads} on the Pt/Pd surface can alleviate CO poisoning and increase the surface density of OH_{ads}, facilitating the oxidation of CO_{ads} to CO_2 (Figure 3c) [46–48]. In addition, selective dopants such as Sn, Ru, and Mo on the Pt/Pd surface can mitigate the bond strength of Pt–/Pd–CO_{ads} by donating charge to Pt/Pd and thus increasing their surface electron density. This electron donor effect enhances the bifunctional mode, which can dramatically improve the MOR performance (Figure 3d) [49].

2.3. Mechanism for Formic Acid Oxidation Reaction (FAOR)

Depending on the catalytic surface, the FAOR can follow two distinct reaction pathways, termed direct and indirect pathways (Figure 4a) [50]. A direct pathway is the direct conversion of HCOOH to CO_2 via dehydrogenation. However, the indirect or dehydration pathway is dominant since Pt–/Pd–COOH, and sequential Pt–/Pd–CO_{ads} are readily formed due to the difficulty of C-O bond cleavage during FAOR. The poisoning of CO_{ads} can be minimized by decorating the catalyst surface with another metal. Dinesh et al. showed the FAOR mechanism on a trimetallic PdRuPt catalyst [51]. Due to the substantial relocation of electrons from Pd and Ru to Pt, the binding energy of Pt–CO_{ads} is suppressed (Figure 4b). Additionally, Ru dopant preferring OH_{ads} can affect the oxidation of Pt–CO_{ads} to CO_2 formation. Thus, the bifunctional mechanism enables the suppression of CO poisoning and hence enhances the FAOR.

2.4. Mechanism for Ethylene Glycol Oxidation Reaction (EGOR)

EGOR is promising for direct alcohol fuel cells due to its high theoretical energy density (10 e^- per molecule) and safer handling compared to methanol. In addition to electricity generation, EGOR can yield value-added C_2 products (e.g., glycolic and oxalic acids), while also serving as a platform to design CO-tolerant catalysts relevant for broader electrocatalysis. Mechanistically, complete oxidation to CO_2 is rarely achieved because O–H bond cleavage is less favorable than C–O cleavage (Figure 4c). In addition, owing to the high activation for C–C bond cleavage, the oxidative products of EG are dominantly C_2 species (glycolaldehyde, glyoxal, glycolic acid, glyoxylic acid, oxalic acid) [42,43,52,53]. Only a tiny amount of EG is oxidized to C_1 species, which are further oxidized to CO and finally to CO_2. The sluggish EGOR can be enhanced by adding metal dopants on Pt or Pd surface. The electron charge donor effect of the metal dopant to Pt/Pd facilitates the breaking of the C–C bond and increases CO tolerance capacity (Figure 4d). Moreover, the bifunctional effect is also observed on metal dopant-containing surfaces to boost EGOR.

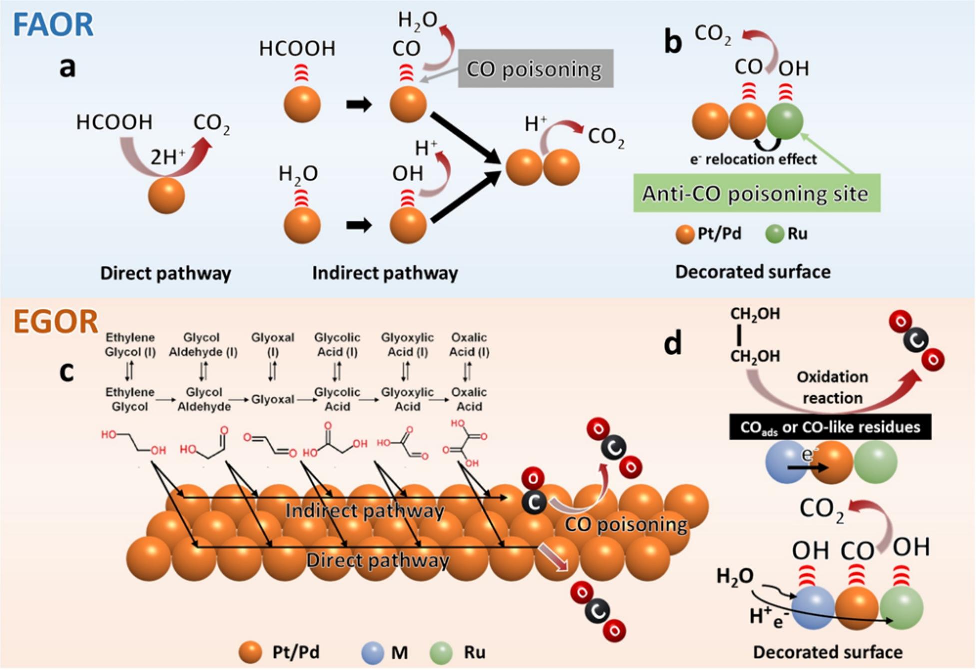

Figure 4. (**a**) Direct and indirect mechanisms of the FAOR on Pd/Pt surface and (**b**) FAOR on dopant-containing surface. Mechanism for EGOR (**c**) on Pt or Pd surface and (**d**) metal dopant-containing surface. Reproduced with permission [54]. Copyright 2009 Elsevier.

3. Protocols for Elemental Doping on Nanosurfaces

Surface doping with metals and metal oxides has become a central strategy for enhancing the electrocatalytic activity of Pt- and Pd-based nanocatalysts in liquid fuel oxidation reactions (LFOR). By tuning surface composition and introducing new active sites, these modifications alleviate CO poisoning and improve reaction pathways. Among the available synthetic approaches, wet-chemical routes are particularly attractive due to their scalability, reproducibility, and precise control over morphology and composition.

Choi et al. demonstrated this strategy by decorating Pt nanocubes with Rh using a two-step wet-chemical process [41]. At low Rh precursor loading, atomically dispersed single Rh sites were formed ($Rh_{at}O$–Pt NCs), whereas higher Rh input led to clustered Rh species ($Rh_{cl}O$–Pt NCs). HAADF-STEM and elemental mapping confirmed the uniform cubic morphology with distinct distributions of Pt, Rh, and O (Figure 5a,b). In-situ EXAFS at the Rh K-edge further revealed Rh–O coordination for the atomically dispersed case, while additional Rh–Rh peaks appeared in the clustered sample (Figure 5c,d). Structural models clearly distinguish isolated Rh–O sites from Rh–O clusters on Pt surfaces (Figure 5e,f).

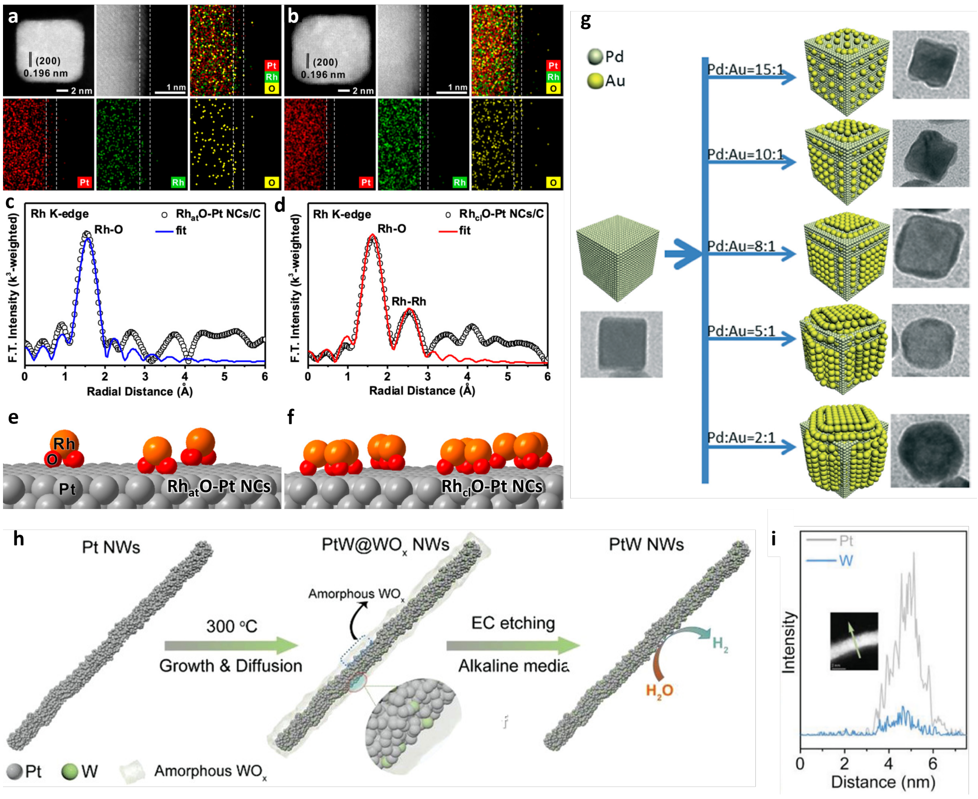

Figure 5. HAADF-STEM images and EDS mapping of (**a**) $Rh_{at}O$-Pt NCs and (**b**) $Rh_{cl}O$-Pt NCs. k^3-weighted Rh K-edge EXAFS spectra of (**c**) $Rh_{at}O$-Pt NCs/C and (**d**) $Rh_{cl}O$-Pt NCs/C. Schematic of (**e**) $Rh_{at}O$-Pt NCs and (**f**) $Rh_{cl}O$-Pt NCs decorated Pt surface obtained from wet-chemical synthesis. Reproduced with permission [41]. Copyright 2022, The National Academy of Sciences. (**g**) Schematic of Au-decorated Pd nanocubes showing the different surface composition. Reproduced with permission [55]. Copyright 2016, The Royal Society of Chemistry. (**h**) Schematic illustration for the decoration on the PtW NWs using electrochemical etching process. (**i**) EDS line mapping profile for W-doped Pt NWs. Reproduced with permission [57]. Copyright 2022, John Wiley & Sons.

Du et al. extended the concept to Pd nanocubes by introducing Au decoration via a seed-mediated method [55]. Pd nanocubes were first synthesized by ascorbic acid reduction and subsequently coated with Au at controlled Pd/Au ratios. The degree of Au coverage strongly influenced morphology: discrete decoration was obtained at 15:1 and 10:1 ratios, more uniform layers at 8:1 and 5:1, and complete surface encapsulation at 2:1. The progressive evolution from sharp cubes to irregular morphologies was clearly observed in TEM and schematic models (Figure 5g). EDS mapping further confirmed Au enrichment on Pd surfaces, and the decorated catalysts showed enhanced ethanol oxidation activity.

Beyond chemical synthesis, electrochemical methods offer dynamic restructuring of catalytic surfaces. Yin et al. produced PdBi–$Bi(OH)_3$ nanochains by solvothermal synthesis followed by electrochemical cycling in alkaline electrolyte [56]. The surface oxidation of Bi introduced abundant OH_{ad} species that promoted CO removal, thereby boosting EOR performance.

Electrochemical etching provides yet another doping route. Electrochemical etching is a process that removes a metal component from the catalyst surface via electrochemical treatment. For example, Huang et al. utilized EC on amorphous WO_x-coated ultrathin PtW nanowires (PtW@AWO$_x$ NWs) to form W-doped PtW NWs [57]. For the synthesis, Pt NWs in OAm solution containing W species were heated at 300 °C to obtain the PtW@AWO$_x$ NWs (Figure 5h). Then, etching was performed on PtW@AWO$_x$ NWs using linear sweep voltammetry in 1.0 M KOH solution for 7 cycles. EDS line scanning revealed that the W was doped on the PtW NWs after EC etching (Figure 5i). Despite the negative reduction potential of W^{6+}/W^0 ($E_0 = -1.1$ V vs. RHE), the WO_x species was reduced to W^0 and doped into Pt NWs. The preformed Pt NWs created strongly reductive species of Pt–H by an autocatalytic surface reduction process, which led to the reduction of W^{6+} to W^0 and finally doped on the surface of Pt NWs.

Together, these studies demonstrate how surface doping through noble metals, oxides, or electrochemical modification enables precise control over catalytic interfaces and enhances resistance to CO poisoning. While electrochemical treatments provide mechanistic insights and dynamic modification, wet-chemical synthesis remains dominant due to its reproducibility and scalability. Integrating both strategies, supported by advanced characterization tools, will be crucial for designing next-generation nanocatalysts with optimized activity and durability for LFOR.

4. Surface Decorated Pt/Pd Catalysts Toward LFOR

The decorated nanocatalysts with anti-CO poisoning sites demonstrated their superior electrocatalytic performance toward LFOR over pure Pt/Pd surfaces. This section discusses the activity, stability, and *in-operando* techniques to electrochemically characterize the catalytic performance of the decorated surfaces toward LFOR. The extensively studied liquid fuels discussed in this paper include methanol, ethanol, formic acid, and ethylene glycol.

4.1. MOR Performance

In direct methanol fuel cell (DMFC), the hydrogen oxidation reaction (HOR) at the anode of proton exchange membrane fuel cells (PEMFCs) is replaced by the MOR. DMFCs are suitable for small portable electronic devices due to their easily exchangeable fuel cartridges, high energy density, and fast charging rate [58–60]. Despite the advantages described above, the practical use of the DMFC is laden with several challenges. One of the major problems is the partial oxidation of the methanol, leading to sluggish oxidation reaction kinetics that reduce the number of transferred electrons [59–61]. Moreover, the partial oxidation of methanol produces CO, which deteriorates the cell performance [62,63].

Nanocatalysts containing anti-CO sites on the surface have been proven to be an effective strategy to address the problem and improve the MOR performance significantly [64,65]. For instance, Lin et al. reported a facile synthesis of Ru-decorated Pt icosahedra and cubes as highly active electrocatalysts for MOR [66]. Ru-decorated Pt catalysts have been identified as a promising candidate for MOR due to their excellent catalytic activity and improved CO tolerance arising from the bifunctional and ligand effects between the two metal elements [67–69]. Figure 6a,b show HAADF-STEM images with atomic resolution and EDX mapping images of the PtRu icosahedron and cube enclosed by (100) and (111) facets, respectively. From the EDX mapping of the icosahedron and cube, Ru (red color) was found to be decorated on the Pt surface (green color), suggesting a Ru-decorated Pt structure. Figure 6c compares the CVs of the catalysts for MOR performed in a solution containing 0.5 M H_2SO_4 and 0.5 M CH_3OH. The higher I_f/I_r value of 1.50 and 2.02 for PtRu icosahedra and cubes than that of a typical PtRu alloy catalyst (Pt_7Ru/C) indicates that the decoration of Ru on the surface of Pt can improve CO tolerance during MOR. Accordingly, the Ru-decorated Pt icosahedra exhibited enhanced specific (0.76 $mA\cdot cm^{-2}$) and mass (74.4 $mA\cdot mg_{Pt}^{-1}$) activities toward MOR, which were about ~6.7 and ~2.2 times higher than those of the Pt_7Ru/C, respectively (Figure 6d). The enhanced performance of the Ru-decorated Pt nanocrystals can be explained by the bifunctional mechanism discussed in Section 2.2 [70,71]. In terms of stability, the Ru-decorated Pt icosahedra showed ~10% current retention (0.05 $mA\cdot cm^{-2}$) and the Pt cubes showed ~5% retention (0.01 $mA\cdot cm^{-2}$) after 2000 s of continuous operation, confirming improved but still limited stability. Although PtRu alloys also exhibit bifunctional behavior, surface Ru decoration provides a greater improvement. This is because Ru atoms in alloys may be buried in the bulk lattice and thus unavailable for catalysis, while surface-decorated Ru remains fully accessible at the reaction interface. Generally, the presence of Ru on the Pt surface can activate the water to form oxygenated species such as OH_{ads} [72]. The OH_{ads} species on Ru sites further oxidize and finally remove the CO_{ads} intermediates on Pt sites, which enhances the electrocatalytic properties of Ru-decorated Pt catalysts towards

MOR. Moreover, Pellicione et al. showed that on a Ru-decorated Pt surface, the removal of CO species on Pt sites is limited, and CO can co-adsorb on Ru sites with OH species through the migration from Pt sites [73]. Oxidation of CO species with co-adsorbed OH species on Ru sites is also a critical step for the enhanced activity towards MOR. This analysis also supports the bifunctional mechanism towards MOR for such Ru-decorated Pt bimetallic catalysts, where surface decoration ensures a higher density of exposed Ru–OH sites compared to alloyed PtRu, thereby enabling more effective CO oxidation.

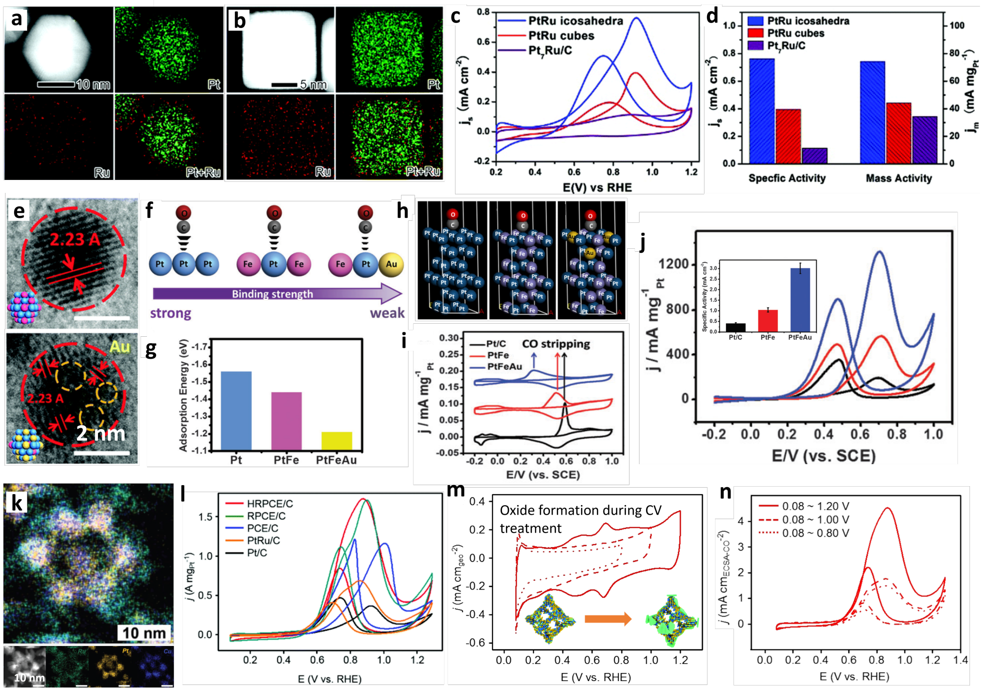

Figure 6. EDX mapping images of (**a**) Ru decorated Pt bimetallic icosahedra and (**b**) Ru decorated Pt bimetallic cubes. (**c**) CV of three different catalysts, including Ru-decorated Pt icosahedra, Ru-decorated Pt cubes, and Pt_7Ru/C for MOR. (**d**) MOR specific and mass activity at the peak position of forward curve. Reproduced with permission [66]. Copyright 2016, The Royal Society of Chemistry. (**e**) HRTEM images of PtFe and PtFeAu nanocrystals, the discontinuous lattice circles of PtFeAu (yellow circles) indicate the decoration of Au atoms. (**f**) Schematic illustration of the binding strength between CO molecule and the Pt centers of Pt, PtFe, and PtFeAu catalysts. (**g**) The model of adsorption of CO on top-site of Pt (111), PtFe (111), and PtFeAu (111). (**h**) Simulation of adsorption energy (E_{ads}) of CO on these three catalysts. (**i**) CO stripping curves of PtFeAu, PtFe, and Pt/C nanocrystals. (**j**) MOR curves of the catalysts in an electrolyte containing 0.5 M H_2SO_4 and 1.0 M CH_3OH. Inset shows the specific activities for MOR. Reproduced with permission [74]. Copyright 2016, The Royal Society of Chemistry. (**k**) HAADF-STEM with EDX mapping images of RuO_x-decorated RuPtCu nanocages. (**l**) CVs of RuO_x-decorated RuPtCu nanocages, state-of-the-art PtRu/C and Pt/C normalized by $ECSA_{CO}$ in solutions containing 0.1 M $HClO_4$ and 1.0 M CH_3OH with a scan rate of 50 $mV \cdot s^{-1}$. (**m**) CVs of RuO_x-decorated RuPtCu nanocages at different potential range in a solution containing 0.1 M $HClO_4$ and (**n**) their corresponding MOR performance [78]. Copyright 2018, The Royal Society of Chemistry.

Surface decoration of a bimetallic alloy with a third metal, forming a trimetallic surface, can also enhance MOR performance. For instance, Cai et al. reported that Au-decorated PtFe nanocatalysts show high resistance to CO poisoning owing to the role of Au as the anti-CO poisoning site [74]. HRTEM images showed the highly crystalline nature of PtFe nanocubes (NCs), whereas the Au-decorated PtFe NCs showed a discontinuous structure (indicated by yellow circles) (Figure 6e). The adsorption energy (E_{ads}) of CO on the (111) plane of bare Pt, Pt_1Fe_1, and $Pt_5Fe_4Au_1$ was calculated (Figure 6f–h), showing that Pt(111) exhibited the highest E_{ads} of −1.56 eV, while the Pt_1Fe_1(111) offered a lower E_{ads} (−1.44 eV). Interestingly, $Pt_5Fe_4Au_1$ reported the reduced E_{ads} of −1.21 eV. The electron charge transfer between the Pt atoms surrounded by Fe and Au atoms resulted in a weaker binding interaction between the CO and the Pt surface [75,76]. The authors proved their claims by conducting CO stripping analysis, showing that the peak potential of ternary PtFeAu (312 mV vs. SCE) is lower by 274 and 201 mV compared to Pt/C and PtFe, respectively. This significant negative shift of Au-decorated PtFe reveals the weakest CO-binding on Pt centers [74,77]. The anti-CO poisoning capacity of Au-decorated PtFe showed a mass activity of 1324 $mA \cdot mg_{Pt}^{-1}$, which was 2.3 and 6.6 times that of PtFe and commercial Pt/C catalysts, respectively (Figure 6j).

Moreover, these Au-decorated PtFe catalysts retained ~35% of their activity (~1.0 $mA\cdot cm^{-2}$) even after 5000 s of operation, indicating superior long-term stability compared to PtFe and Pt/C.

Metal oxides can also improve the CO tolerance capability when utilized as a dopant on the Pt surface. For instance, Park et al. reported the CO-tolerant RuO_x decorated RuPtCu trimetallic nanocages (HRPCE/C) with highly improved MOR performance [78]. Representative HAADF- STEM with EDX mapping images of RuO_x decorated ternary nanocages are shown in Figure 6k. Since the OH (OH_{ad}) adsorbed on RuO_2 sites adjacent to Pt could promote the CO tolerance, MOR activity was expected to be enhanced [79–81]. For this, MOR activities of HRPCE/C, state-of-the-art PtRu/C, and Pt/C were recorded in solutions containing 0.1 M $HClO_4$ and 1.0 M CH_3OH with a scan rate of 50 $mV\cdot s^{-1}$ from 0.08 to 1.29 V (vs. RHE) (Figure 6l). The MOR mass activity of HRPCE/C (1.73 $A\cdot mg^{-1}$) was about 2.5 and 5 times that of PtRu/C (0.69 $A\cdot mg^{-1}$) and Pt/C (0.37 $A\cdot mg^{-1}$), respectively. In order to understand the role of RuO_2, the authors controlled the amount of RuO_2 formed on the surface of the catalyst by conducting CV cycling at different potential ranges (Figure 6m). When the HRPCE/C was pre-cycled at a vertex potential of 1.20 V (vs. RHE), a larger amount of RuO_2 was formed, resulting in the specific activity of 4.52 mA cm^{-2}, which was 2.6 and 3.1 times higher than the catalysts pre-cycled at 0.80 V (1.76 $mA\cdot cm^{-2}$) and at 1.00 V (1.48 $mA\cdot cm^{-2}$) (Figure 6n), respectively. Importantly, these RuO_x-decorated RuPtCu nanocages maintained ~19% activity (~0.8 $mA\cdot cm^{-2}$) even after 4000 s of testing, highlighting their stable long-term performance. The authors concluded that the enhanced MOR performances of HRPCE/C are linked to the synergy between the decorated RuO_2 and Pt sites [78]. A comparison of the MOR performance of the catalysts, including stability, is listed in Table 2. These results demonstrate that the MOR performance can be significantly improved by enhancing the anti-CO poisoning capability by decorating a suitable third metal atom on the surface.

Table 2. Comparison of MOR performance of various decorated nanocatalysts.

Catalyst	MA [a] ($A\cdot mg_{Pt/Pd}^{-1}$)	MA Enhancement vs. Pt/C	SA [b] ($mA\cdot cm^{-2}$)	SA Enhancement vs. Pt/C	CA Stability [c]	Electrolyte	Ref.
Ru-decorated Pt cubes	0.41	~3	0.42	~2	~5% (0.01 $mA\cdot cm^{-2}$) activity retention after 2000 s	0.5 M CH_3OH + 0.5 M H_2SO_4	[66]
Ru-decorated Pt icosahedra	0.75	~5	0.76	~4	~10% (0.05 $mA\cdot cm^{-2}$) activity retention after 2000 s	0.5 M CH_3OH + 0.5 M H_2SO_4	[66]
Pt decorated Ru NWs	0.36	4	0.36	3	N/A	0.5 M CH_3OH + 0.1 M $HClO_4$	[82]
Au-decorated PtFe	1.32	6.6	3.01	7.34	~35% (~1.0 $mA\cdot cm^{-2}$) activity retention after 5000 s	0.5 M CH_3OH + 0.5 M H_2SO_4	[74]
Au decorated PtNi	1.48	5	3.84	2	~10% activity retention after 4000 s	1.0 M CH_3OH + 0.5 M H_2SO_4	[49]
RuO_x-decorated RuPtCu nanocages	1.73	5	4.52	8	~19% (~0.8 $mA\cdot cm^{-2}$) activity retention after 4000 s	1.0 M CH_3OH + 0.1 M $HClO_4$	[78]

[a] Mass activity, [b] Specific activity, [c] Chronoamperometry.

The recent progress in decorated Pt/Pd catalysts clearly shows that surface dopant engineering is a powerful strategy for enhancing MOR activity and CO tolerance. In particular, surface-exposed dopants, compared to alloyed or buried atoms play a significant role by supplying abundant OH_{ad} species and weakening CO adsorption. However, long-term stability remains a major limitation, as most catalysts still show decreased activity under continuous operation. In this view, future MOR catalysts should prioritize stabilizing the dopant-Pt interface, preventing dissolution, and maintaining accessible bifunctional sites.

4.2. EOR Performance

Ethanol is often discussed as a promising fuel candidate for the large-scale applications of fuel cells due to its high energy density (Table 1), low toxicity, and easy storage and transportation for practical uses compared to H_2 gas; however, its practical feasibility is still under active investigation [83,84]. Though pure Pt/Pd nanocatalysts are usually utilized for EOR, CO poisoning during EOR severely affects their durability performance. Therefore, a series of modifications to pure Pt/Pd surface by adding transition metals as co-catalysts in various structures and compositions, including adatoms, adlayers and intermetallic Pt–M assemblies, bimetallic alloys, metal oxides, and core-shell nanostructures were introduced to improve EOR performance [9,78,85–89]. However, those Pt-/Pd-based catalysts could not perform the total oxidation of ethanol to CO_2 at moderate positive potentials and were poisoned by CO species over time [90–92]. These led to the investigation of decorating pure Pt or Pd surface with metal dopants as anti-CO sites. For example, Zhong et al. demonstrated that the EOR activity of Au-decorated Pd heterogeneous nanocubes strongly depends on Pd/Au molar ratios ranging from 15:1 to 8:1 (Figure 7a,b) [55]. Their results indicated that Pd_5Au_1 exhibited the highest EOR mass activity which is around 2.2 times higher than that of monometallic Pd. The possible EOR enhancement was due to the addition of Au to Pd nanocubes, resulting in a tensile strain in the structure of the surface of Pd and an upper shift in the d-band center of Pd [93,94]. It was also reported that the improved OH^- adsorption onto the surface of the catalyst promoted the elimination of ethoxy intermediates from the catalyst surface and enhanced EOR performance [95]. They also suggested that the optimal ratio of Pd_5Au_1 showed a higher ECSA value due to the presence of more active sites, which might significantly affect EOR. Therefore, it is expected that maximum EOR can be achieved by decoration and optimal surface composition. However, Pd–Au catalysts still showed limited durability, with only ~5% activity retained after 2000 s.

Occasionally, a stable surface is projected to behave as an excellent catalytic site for EOR. The surface decoration strategy, including heterogeneous atomic doping, can stabilize the initial morphology and prevent the loss of transition metals during electrocatalysis. In particular, morphology such as one-dimensional (1D) nanowires (NWs) can benefit from surface decoration due to its exceptional surface area and intrinsic activity to improve catalytic performance. For example, Li et al. investigated lavender-like Ga-doped Pt_3Co NWs on EOR, where optimized surface energy derived from the doping of Ga atoms improved EOR activity [96]. The surface energy of the Ga-doped Pt_3Co (111) surface was measured and further compared to the Pt_3Co (111) and pure Pt surfaces (Figure 7c). Surface energy indicates an approximate measure of energetic surface stability and the lower the surface energy, the more stable the catalyst's surface. The surface energy of the Pt_3Co was calculated to be 1.29 $J \cdot m^{-2}$, which is 11% lower than that of the pure Pt surface (1.45 $J \cdot m^{-2}$). Interestingly, doping of Ga into the Pt_3Co surface further lowers its surface energy to 1.17 $J \cdot m^{-2}$, rendering the Ga-doped Pt_3Co surface even more stable. Yuge et al. showed that the stable alloy surfaces exhibited weaker CO binding compared to the pure Pt surface [94]. Therefore, Ga doping on Pt_3Co surface can act as anti-CO poisoning sites for improved EOR performance. Consequently, the 4% Ga–Pt_3Co/C delivered the highest electrocatalytic performance with a specific activity of 4.2 $mA \cdot cm^{-2}$ and a mass activity of 2.0 $A \cdot mg^{-1}$, respectively (Figure 7d). Moreover, Ga–Pt_3Co NWs retained ~60% of their activity after 36,000 s, highlighting their remarkable durability. Mao et al. reported the Mo-doped PtNi NWs with a diameter of ~2.5 nm, where the addition of Ni produces surface defects and Mo can stabilize Ni and Pt atoms, leading to superior EOR performance [97]. The incorporation of 3d transition metals (Ni) into the Pt lattice to form ternary Pt–Mo–Ni NWs can promote the adsorption of hydroxyl species from water and remove the poisoned CO intermediates at a lower potential compared to Pt/C catalysts. Spatial confinement and energetic preference allow Mo to be permanently retained in Pt–Ni NWs. Hence, the subsurface Mo atoms will increase the cohesive atomic energies of the Ni by 0.27 eV and the Pt by 0.29 eV. This indicates that Mo has a stabilizing effect on undercoordinated sites of Pt–Ni NWs, which are the available sites for reactions.

In addition, Pt/Pd-based nanocatalysts with trimetallic surfaces exhibited more anti-CO poisoning properties than bimetallic surfaces due to the electron charge donor effect, accelerated C–C bond cleavage, and improved selectivity to CO_2 formation. For example, Dai et al. showed a set of earth-abundant elements, namely group IIIA and IVA metals (Ga, In, Sn, Pb) and late 3d transition metals (Fe, Co, Ni, Cu) to partially dope the noble metals such as Pt and Rh surface for the construction of trimetallic Pt–Rh–M nanoalloys and to uncover their EOR reactivity and CO_2 selectivity [38]. For those alloyed systems, a representative trimetallic Pt_3RhSn/C catalyst is considered, where HAADF-STEM and EDS line mapping demonstrated that the Pt_3RhM/C catalysts shared similar elemental distributions (Figure 7e). Pt_3RhSn/C is reported to show 67 and 7 times increment in EOR specific activity and mass activity, respectively, at 0.45 V (vs. RHE) compared with a commercial Pt/C catalyst in acidic conditions (Figure 7f). The group investigated the intermediates and products of EOR utilizing the in-situ FTIR (Figure 7g–i). Catalysts were typically swept at a potential ranging from 0.15 V to 0.95 V. The signature peak of CO_2 (2343 cm^{-1}) corresponds to the complete oxidation of ethanol, which indicates the breakage of the C–C bond in ethanol. Among those reported Pt–Rh–M catalysts, the early CO_2 peak implied that Pt_3RhSn/C performed complete EOR at low potential. The anti-CO poisoning property of Pt_3RhSn/C was also observed as there was no linearly adsorbed CO (CO_L) located at 2047 cm^{-1}, suggests that the adsorption of poisonous CO_L was weakened by the optimized electronic structure of Pt_3RhSn/C (Figure 7i).

An abundant source of OH_{ads} species resulting from decorated metals can accelerate the removal of adsorbed CO species from the surface. Therefore, the superior anti-CO poisoning species on the surface can also offer a catalytic boost for EOR performance by facilitating the oxidative removal of carbon-containing species. Following this concept, Yuan et al. reported $Bi(OH)_3$ decorated PdBi nanochains where strongly coupled $Bi(OH)_3$ played an important role in determining the anti-poisoning property [56]. The OH_{ad} species formed on $Bi(OH)_3$ paved an efficient way to accelerate the oxidative removal of CO or other intermediates on Pd active sites (Figure 7j). CO stripping analysis in the range from 0.7 to 0.8 V indicates that the onset potential of CO oxidation on PdBi-$Bi(OH)_3$ nanochains shifted 100 mV in the negative direction compared to that of Pd/C, indicating the Pd d-band center was downshifted (Figure 7k). The EOR performance of PdBi–$Bi(OH)_3$ and Pd/C was evaluated in 1 M NaOH containing 1 M ethanol, as shown in Figure 7l. The ratio between the intensity of the forward scan peak (I_f) and the reverse scan peak (I_r) relates to the degree of EOR and the tolerance toward CO poisoning [96]. The I_f/I_r value of PdBi–$Bi(OH)_3$ nanochains was nearly 2.5, which was much higher than that of Pd/C (0.9), indicating a more robust tolerance against poisoning by intermediate species (Figure 7l) [56].

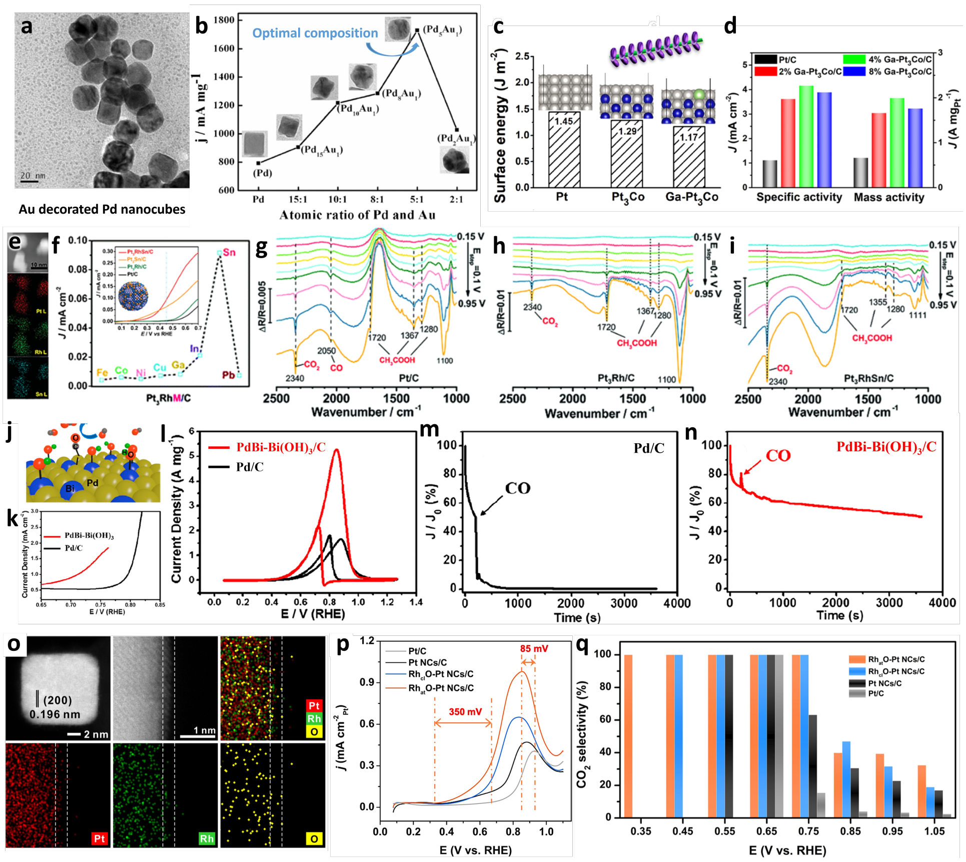

Figure 7. (**a**) TEM images of Au-decorated Pd nanocubes (Pd_5Au_1) and (**b**) relationship between the composition of the catalysts and their corresponding EOR mass activity. Reproduced with permission [55]. Copyright 2016, The Royal Society of Chemistry. (**c**) Surface energy of pure Pt, Pt_3Co, and Ga-doped Pt_3Co (111) surfaces. Gray, blue, green, and red spheres represent Pt, Co, Ga, and O atoms, respectively. (**d**) Specific activities and mass activities of different Ga-doped Pt_3Co NWs and commercial Pt/C catalysts in 0.1 M $HClO_4$ containing 0.5 M CH_3CH_2OH. Reproduced with permission [96]. Copyright 2020, American Chemical Society. (**e**) HAADF–STEM–EDS mapping scans (right side) of Pt_3RhSn/C catalyst. (**f**) EOR curves of trimetallic Pt–Rh–M nanoalloys and their specific activities at 0.45 V. In-situ FTIR spectra recorded during the EOR on (**g**) Pt/C, (**h**) Pt_3Rh/C, and (**i**) Pt_3RhSn/C at continuous stepped potentials from 0.15 V to 0.95 V in a mixture containing 0.1 M $HClO_4$ and 0.5 M CH_3CH_2OH. Reproduced with permission [38]. Copyright 2018, The Royal Society of Chemistry. (**j**) Schematic illustration of the oxidative removal mechanism of CO on PdBi–$Bi(OH)_3$ nanochains sites in which yellow, blue, red, green, and gray spheres represent Pd, Bi, O, H, and C, respectively. (**k**) Enlarged CO-stripping curves at potentials from 0.65 to 0.85 V. (**l**) EOR performances of PdBi–$Bi(OH)_3$ nanochains and commercial Pd/C catalysts in 1 M NaOH containing 1.0 M CH_3CH_2OH. Chronoamperometric response of (**m**) commercial Pd/C and (**n**) PdBi-$Bi(OH)_3$ nanochains in a solution of 1 M NaOH containing 1 M ethanol at 0.86 V. CO gas was purged into the electrolytes at 200 s. Reproduced with permission [56]. Copyright 2019, American Chemical Society. (**o**) CV profiles of the synthesized electrocatalysts measured in Ar-saturated 0.1 M $HClO_4$ solution. (**p**) EOR curves of $Rh_{at}O$-Pt NCs and commercial Pt/C catalysts in 0.1 M $HClO_4$ containing 0.2 M CH_3CH_2OH. (**q**) The CO_2 selectivity of all samples ranging from 0.25 to 1.05 V obtained from in-situ IRRAS spectra. Reproduced with permission [41]. Copyright 2022, The National Academy of Sciences.

The mass normalized current density of PdBi–Bi(OH)$_3$ nanochains was 5.30 A·mg$_{pd}^{-1}$, which was 4.6 times higher than that of Pd/C. The authors also tried to demonstrate the enhanced CO tolerance of PdBi-Bi(OH)$_3$ during EOR by purging CO gas into the electrolytes at 200 s (Figure 7m,n). The poor CO tolerance for commercial Pd/C was observed as the EOR current density swiftly dropped to zero. On the other hand, PdBi–Bi(OH)$_3$ sample showed superior tolerance as 50% of the EOR current density could still be observed after 3600 s. In addition, the authors showed that the PdBi–Bi(OH)$_3$ could be reactivated electrochemically in a fresh electrolyte after each 20,000 s stability test. After reactivation, PdBi–Bi(OH)$_3$ could retain its original EOR activity. It was concluded that Bi(OH)$_3$ decoration can act as an anti-CO poisoning site which enhances the activity and stability of the EOR process. The high EOR activity and excellent stability made PdBi–Bi(OH)$_3$ one of the best reported EOR electrocatalysts.

Metal dopants can also act as the active component for complete EOR process. For example, Qiaowan et al. showed that partially oxidized Rh decorated on the Pt nanocube surface could completely oxidize ethanol to CO$_2$ at a record-breaking low potential of 0.35 V. A controlled decoration of partially oxidized single Rh on the (100) surface of Pt nanocubes (Rh$_{at}$O-Pt NCs) was achieved (Figure 5a) [41]. CV curves showed Pt NCs/C with typical Pt(100) H adsorption/desorption (0.08–0.45 V vs RHE). Rh$_{at}$O-Pt NCs/C exhibited Pt–O (0.75–1.0 V) and Rh–O (0.45–0.65 V) reduction peaks, while Rh$_{cl}$O-Pt NCs/C lacked Pt–O reduction, indicating an Rh-dominated surface (Figure 7o). EOR analysis indicates that compared to Pt/C, the Rh$_{at}$O-Pt NCs/C nanocatalyst showed negative shifts of the main peak and EOR onset potentials by 85 and 350 mV, respectively (Figure 7p). Additionally, the EOR current densities of Rh$_{at}$O-Pt NCs/C showed 11.4 times more enhancement than Pt/C at 0.75 V (Figure 7p). The role of Rh doping was unveiled by infrared reflection absorption spectroscopy (IRRAS). From the IRRAS peak integration, EOR products were quantitatively determined at a potential range of 0.35 to 1.05 V (Figure 7q). The Rh decoration remarkably improved the CO$_2$ selectivity. The Rh$_{at}$O-Pt NCs/C catalyst showed CO$_2$ selectivity of >99.9% from 0.35 to 0.75 V, revealing its strong C–C bond scission ability of ethanol in a wide range of potentials. From the IRRAS results, the authors concluded that Rh is the active component for C–C bond scission in ethanol, while Pt is the active center for the overall EOR performance. Therefore, Rh–O–Pt has the combination of EOR activity of Rh and Pt and assists in the formation of OH$_{ad}$, which removes the adsorbed CO$_{ad}$. Finally, as shown in Table 3, decorated nanocatalysts demonstrated superior EOR performances compared to commercially available Pt/Pd nanocatalysts.

Table 3. Comparison of EOR performance of various state-of-the-art decorated nanocatalysts.

Catalyst	MA [a] (A·mg$_{Pt/Pd}^{-1}$)	MA Enhancement vs. Pt/C	SA [b] (mA·cm^{-2})	SA Enhancement vs. Pt/C	CA Stability [c]	Electrolyte	Ref.
Au-decorated Pd	1.74	2.2 (vs. Pd)	2.85	~1	~5% (0.02 A·mg^{-1}) activity retention after 2000 s	1.0 M C$_2$H$_5$OH + 1.0 M KOH	[55]
Pt$_3$RhSn	0.02	7	0.09	67	~10% (0.01 mA·cm^{-2}) activity retention after 36,000 s	0.5 M C$_2$H$_5$OH + 0.1 M HClO$_4$	[38]
Ga-doped Pt$_3$Co NWs	2.00	4	4.20	4	59.8% (0.01 mA·cm^{-2}) activity retention after 36,000 s	0.5 M C$_2$H$_5$OH + 0.1 M HClO$_4$	[96]
Mo-doped PtNi NWs	0.87	6.3	2.57	13.4	~17% (0.4 mA·cm^{-2}) activity retention after 1500 s	2.0 M C$_2$H$_5$OH + 0.5 M H$_2$SO$_4$	[97]
Ni(OH)$_2$ decorated Pt–Cu octahedra	1.97	5	8.40	~13	N/A	1.0 M C$_2$H$_5$OH + 0.1 M HClO$_4$	[98]
Bi(OH)$_3$ decorated PdBi nanochains	5.30	4.6 (vs. Pd/C)	N/A	N/A	36% (1.00 A·mg^{-1}) activity retention after 20,000 s	1.0 M C$_2$H$_5$OH + 1.0 M NaOH	[56]
SnO$_2$ patched ultrathin PtRh NWs	3.16	5.3	5.63	4.3	~10% (0.05 A·mg^{-1}) activity retention after 1000 s	1.0 M C$_2$H$_5$OH + 1.0 M NaOH	[99]
SnO$_2$ decorated PtRhNi nanoframes	0.13	6	0.72	10	~20% (0.03 A·mg^{-1}) activity retention after 1500 s	0.5 M C$_2$H$_5$OH + 0.1 M HClO$_4$	[100]
Single Rh decorated Pt nanocubes	0.21	5	0.73	11.4	~24% activity retention after 600 s	0.2 M C$_2$H$_5$OH + 0.1 M HClO$_4$	[41]

[a] Mass activity, [b] Specific activity, [c] Chronoamperometry.

Surface decoration has proven to be one of the effective routes for improving EOR kinetics by facilitating C–C bond cleavage, enhancing OH$_{ad}$ availability, and suppressing CO poisoning intermediates. This review summarized that electronic modulation of the Pt/Pd surface can dramatically shift reaction pathways toward complete EOR oxidation. However, achieving high CO$_2$ selectivity at low potentials while maintaining long-term stability remains challenging. We believe that future research should focus on new metal dopant that stabilize active facets, suppress metal leaching, and enable rapid desorption of carbonaceous intermediates.

4.3. FAOR Performance

Direct formic acid fuel cells (DFAFCs) are regarded as one of the most promising liquid fuel cells due to the high power densities, nontoxicity, and low fuel crossover through the Nafion membrane [9,101–104]. Pt-/Pd-based catalysts have been considered the most suitable catalyst for the anodic FAOR in DFACFs. FAOR proceeds on the surface Pt and Pd through a widely accepted dual-path mechanism [105–107]. A detailed mechanism has been discussed in Section 2, which revealed that decorated metal and metal oxide species could play a key role as anti-CO poisoning species during FAOR. Moreover, in acidic conditions, monometallic Pd and Pt catalysts suffer from deactivation and shape deformation during FAOR. Surface decoration can improve activity, preserve the shape, and enable superior stability during FAOR. For instance, Rettenmaier et al. reported SnO_2 decorated Pd (SnO_2@Pd) NCs, improving the electrocatalytic FAOR activity compared to Pd NCs due to a decrease in the oxidizing potential of CO intermediates while maintaining the Pd sites free of poisoning [108]. Figure 8a shows HRTEM images of SnO_2@Pd NC supported on carbon powder where the SnO_2 agglomerates were found on Pd cubes. The authors demonstrated that with SnO_2 decoration, the Pd oxidation state does not change during FAOR. To support their claim, the authors conducted *in-operando* X-ray absorption fine structure (XAFS) measurements during FAOR to obtain the chemical state of Pd and Sn (Figure 8b–d). The X-ray absorption near edge structure (XANES) analysis at the Sn K-edge (Figure 8b) reveals that the local structure and oxidation state around Sn in the SnO_2@Pd NC catalyst can be related to the SnO_2 reference material, and no change occurred during the FAOR operation. An analysis of the Pd K-edge data in Figure 8c indicates that the Pd oxidation state and local structure do not alter during FAOR, revealing superior stability SnO_2@Pd NC during FAOR. It was also revealed that Pd in the Pd NCs and SnO_2@Pd NCs catalysts were in a reduced state and matched with metallic fcc-Pd. Similar to the XANES data analysis, the Fourier-transform extended X-ray absorption fine structure (FT-EXAFS) analysis (Figure 8d) revealed that before the FAOR and during the FAOR, catalysts are in the reduced state and match with a local structure similar to that of pure metallic Pd. This analysis shows that the decorated SnO_2 can stabilize the Pd surface and the electron relocation effect remains intact during and after FAOR. As a result, the SnO_2@Pd NC exhibited good FAOR performance, as revealed by the CV (Figure 8e).

From the CV, the peak potential for SnO_2@Pd NCs was found at 0.55 V (vs. RHE), which was shifted by 100 mV lower potential than that of Pd NCs. SnO_2@Pd NCs showed a 5.8-fold enhanced current density at 0.55 V (vs. RHE) compared to the Pd NCs. Moreover, the authors performed in-situ FTIR during FAOR and compared the CO_2 evolution (Figure 8f–h). The vibrational frequency of dissolved CO_2 was recorded at 2345 cm^{-1} (C–O stretch) [109]. It can be seen that the CO_2 signal generated from FAOR starts to evolve at 0.21 V for Pd NCs (Figure 8f), while the CO_2 signal can be observed at 0.01 V for the SnO_2@Pd NCs (Figure 8g). Interestingly, the advantages of in-situ FTIR measurements for FAOR can be realized as the onset potentials for the catalytic activities were 140 mV lower than the onset potentials measured by the CV technique (Figure 8h). This analysis reveals the higher sensitivity of the in-situ FTIR measurements for FAOR, which can be utilized for detecting the catalytic activity of SnO_2@Pd NC at a lower potential.

The superior FAOR performance of the catalyst was also attributed to improved CO tolerance. Therefore, the authors have demonstrated CO stripping analysis to evaluate the anti-CO properties of the catalyst utilizing conventional CO stripping analysis and in-situ FTIR analysis. From the CO stripping analysis (Figure 8i), similar peak potentials were observed for both the catalysts (0.86 V), suggesting the absence of strain effect by decorating SnO_2 on the Pd lattice. Interestingly, the onset potential for CO oxidation was lower for SnO_2@Pd NCs (0.61 V) than Pd NCs (0.73 V). The potential was lowered due to the oxophilic sites providing oxygen at a lower Sn oxidation potential. Also, the oxidative current in the potential range of 0.6 to 1.0 V (vs. RHE) indicates a more facile CO oxidation, surface heterogeneity, and a slower CO surface diffusion toward the reactive Pd sites on SnO_2@Pd NCs [110–113]. Additionally, the vibrational frequency of bridge-bonded CO_B (C–O stretch) is recorded between 1900–1955 cm^{-1}. In the case of Pd NCs (Figure 8j), the CO_B band primarily appears at 1945 cm^{-1} and starts shifting as the potential changes from 1951 cm^{-1} (0.16 V) to 1958 cm^{-1} (0.71 V). The shifting is also observed for SnO_2@Pd NCs (Figure 8k), but the peak intensity starts to decline at 0.66 V (vs. RHE), suggesting the earlier CO oxidation of the SnO_2@Pd NCs. The integrated band intensities of the CO_2 formation in Figure 8l also suggest the lowered onset potential for SnO_2@Pd NCs (0.66 V) than Pd NCs (0.71 V), matching with previous CO stripping data.

Scofield et al. reported ultrathin Fe-doped PtRu NWs and utilized the decorated material toward FAOR [114]. They prepared several PtRuFe compositions and investigated their performance toward MOR and FAOR. Among those prepared ultrathin Fe-doped PtRu NWs catalysts, $Pt_7Ru_{1.5}Fe_{1.5}$ NWs showed the highest FAOR performance. The authors concluded that the corresponding Fe content primarily impacts FAOR within the ternary metal alloy nanowire. Vidal-Iglesias et al. reported that the highest FAOR could be achieved for Pt(100) electrodes decorated by Pd adatoms, owing to the decreased CO poisoning and the lowering of the onset potential for FAOR at 0.12 V (vs. RHE) [115]. A comprehensive FAOR performance comparison of previously reported catalysts with the metal-doped surface is shown in Table 4.

Decorated Pt/Pd catalysts have shown clear advantages in FAOR by lowering CO oxidation potentials, stabilizing active surfaces, and preserving the morphology of the catalysts during extended operation. These findings confirm that controlled electronic tuning of the surface can shift the FAOR pathway toward efficient dehydrogenation while minimizing poisoning. Future studies should include a deeper integration of in-situ/operando XAFS, FTIR, and SEIRA techniques to directly correlate surface chemistry with FAOR activity.

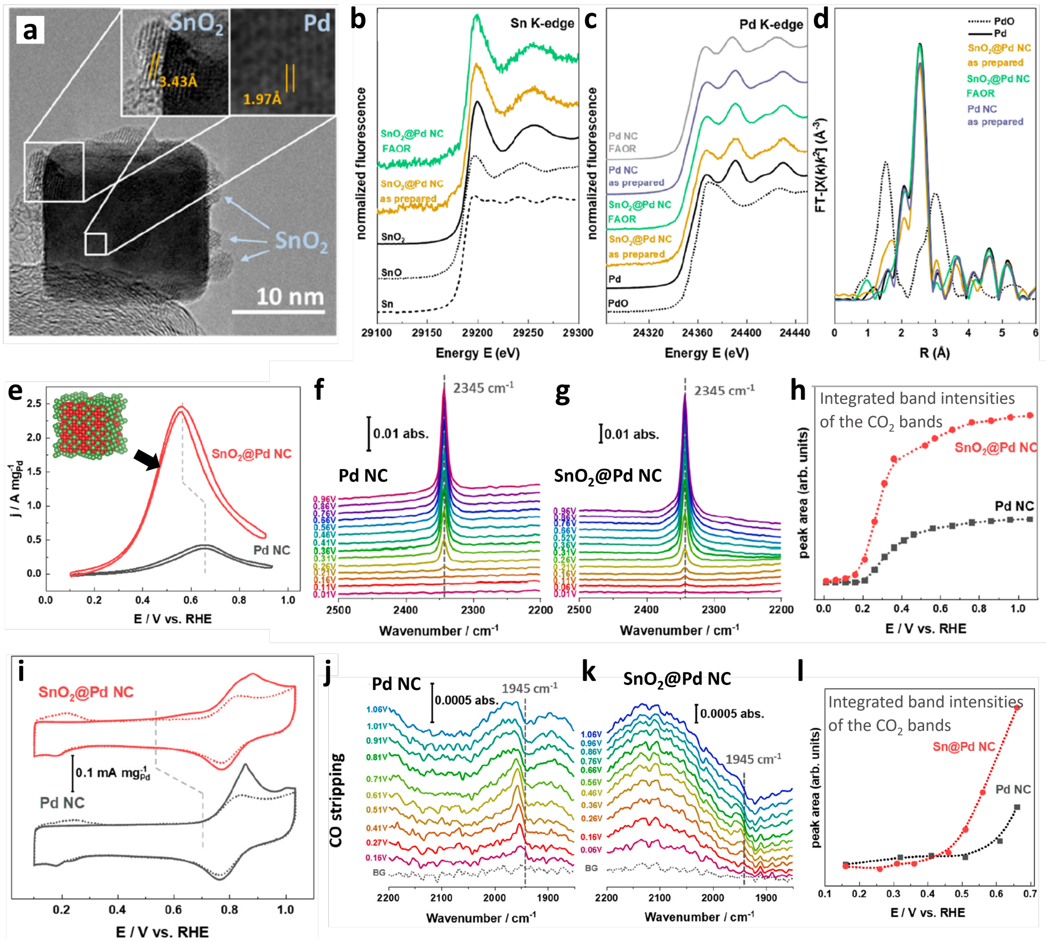

Figure 8. (**a**) HRTEM images of SnO2@Pd NCs. XANES spectra at the (**b**) Sn K-edge of SnO2@Pd NCs and (**c**) Pd K-edge for the Pd NCs, and SnO2@Pd NCs in the as-prepared state and *in-operando* spectra collected during 3 h of the FAOR in 0.1 M $HClO_4$ + 0.5 M HCOOH at 0.45 V vs. RHE. (**d**) Fourier-transformed (FT) k2-weighted Pd K-edge EXAFS spectra for both catalysts in the as-prepared state and during the reaction. (**e**) CV for FAOR of the SnO2@Pd NC and Pd NC (gray) in 0.1 M $HClO_4$ + 0.5 M HCOOH at 50 $mV\cdot s^{-1}$. In-situ FTIR of FAOR showing CO_2 bands during FAOR for (**f**) Pd NCs and (**g**) SnO2@Pd NCs; (**h**) integrated band intensities of the CO_2 bands during FAOR. Reference spectra were taken at −0.04 V vs. RHE on glassy carbon electrode in 0.1 M $HClO_4$ and 25 mM HCOOH. (**i**) CO-stripping voltammograms of SnO2@Pd catalysts (red) and Pd catalysts (gray) in 0.1 M $HClO_4$ at 20 $mV\cdot s^{-1}$. In-situ FTIR of the CO-stripping experiments in the CO regime of (**j**) Pd NCs and (**k**) SnO2@Pd NCs; (**l**) integrated intensities of the corresponding CO_2 bands. Reference spectra taken at 0.06 V vs. RHE taken on Au foil in 0.1 M $HClO_4$. Reproduced with permission [108]. Copyright 2020, American Chemical Society.

Table 4. Comparison of FAOR performance of various decorated nanocatalysts.

Catalyst	MA [a] ($A\cdot mg_{Pt/Pd}^{-1}$)	MA Enhancement vs. Pt/C or Pd/C	SA [b] ($mA\cdot cm^{-2}$)	SA Enhancement vs. Pt/C or Pd/C	CA Stability [c]	Electrolyte	Ref.
SnO_2 decorated Pd cubes	2.46	5.8	27	~5	~60% mass activity retention after 10,800 s	0.5 M HCOOH + 0.1 M $HClO_4$	[108]
Fe-doped PtRu NWs	N/A	N/A	2.15	4 (Pt NWs)	N/A	0.5 M HCOOH + 0.1 M $HClO_4$	[114]
Au decorated PtNi	3.44	9.5	4.54	2.52	~40% mass activity retention after 4000 s	0.5 M HCOOH + 0.1 M $HClO_4$	[49]
Pd adatom decorated Pt	N/A	N/A	~1.5	~5	~20% specific activity retention after 600 s	0.1 M HCOOH + 0.5 M H_2SO_4	[115]
Pt decorated PdFe	1.93	1.52 (vs. 1.52)	N/A	N/A	~20% mass activity retention after 2100 s	0.5 M HCOOH + 0.1 M $HClO_4$	[110]
Sn-doped PdCu	2.42	3.94	N/A	N/A	102.3 times mass activity than Pd/C after 3600 s	0.5 M HCOOH + 0.5 M H_2SO_4	[116]
(Y–Pt)–$PtTe_2$ HPNT/C	6.4	49.2	5.4	25.7	~80.4% mass activity retention after 36,000 s	0.5 M HCOOH + 0.5 M H_2SO_4	[117]
Sb-decorated Pt octahedral NPs	NA	NA	~2.8	NA	88% mass activity retention after 600 s	0.5 M HCOOH + 0.5 M H_2SO_4	[118]

[a] Mass activity, [b] Specific activity, [c] Chronoamperometry.

4.4. EGOR Performance

Ethylene glycol (EG), produced from cellulose, is an attractive energy carrier for electrocatalytic applications. Due to its high boiling point of 198 °C, coupled with theoretical capacity (4.8 Ah/mL) and a higher boiling point than methanol (64.7 °C), it renders an advantageous and safe candidate alternative to methanol and ethanol, which can be fed in direct alcohol fuel cells [54,119,120]. In addition, EG is less volatile than ethanol, reducing raw-material wastage [121]. Pt has been considered a promising electrocatalyst for EGOR, and there are two pathways for EGOR, which we have discussed in chapter 2.4 [42,122,123]. However, one pathway will lead to poisoning the catalyst surface and making the Pt surface inactive for further reaction. These led to studies on surface decoration protocols with various metal atoms, which not only enhance the EGOR but also act as anti-CO sites for long-time stability of EGOR.

One current strategy to improve the electrocatalytic activity of Pt is to generate a catalytic surface with high-index facets (HIFs). Reports reveal that HIFs with high-density steps and kinks improve LFOR by lowering the potential for CO oxidation [124–127]. For example, Wang et al. unveiled that doping non-noble metal or nonmetals into the near-surface of the Pt-based nanocrystals bound with HIFs exhibits high activity and stability toward EGOR [124]. The metal dopant in the catalytic surface of Pt can change the electrochemical properties. Furthermore, the metal dopants also assist in stabilizing the crystal surface structure of Pt-based nanocrystals. The group also reported Mo doping on the HIF of Pt_3Mn catalyst, which showed advantages such as easier C–C cleavage of EG, the direct conversion of carbonaceous species to CO_2, and suppressing CO_L poison formation species [128]. A schematic illustration of Mo-doped Pt_3Mn is shown in Figure 9a, where the Mo component is doped into the surface lattice of Pt_3Mn outer layer.

EGOR analysis for different Mo-doped Pt_3Mn and commercial Pt/C was conducted in 0.1 M $HClO_4$ solution containing 0.5 M EG. It was found that the specific activities (Figure 9b) of 1.8%Mo/Pt_3Mn, 0.4%Mo/Pt_3Mn, and 0.07%Mo/Pt_3Mn were 0.95, 1.23, and 0.86 $mA\cdot cm^{-2}$, which are 2.2, 2.9, and 2.0 times higher than that of Pt_3Mn catalyst (0.43 $mA\cdot cm^{-2}$), respectively. It is evident from the above results that an optimum amount of Mo doping is necessary for maximizing EGOR performance. In-situ FTIR spectroscopy was utilized to measure the effects of Mo doping for EGOR performance in 0.1 M $HClO_4$ + 0.5 M EG solution, and the results are displayed in Figures 9c and d, for Pt_3Mn and 0.4% Mo-doped Pt_3Mn, respectively. The negative band at 2343 cm^{-1} represents the CO_2 formation found after applying more than 0.6 V (vs. RHE) [129,130]. Moreover, the band observed at about 2050 cm^{-1} corresponds to the linearly bonded CO (CO_L) [130–132], which was undetectable for 0.4% Mo-doped Pt_3Mn, confirming that the formation of CO was deterred. Therefore, no signals of CO_L in 0.4% Mo-doped Pt_3Mn spectra imply that the catalyst follows a direct pathway where the C_1 species are directly oxidized to CO_2 without forming CO_L species. To confirm the above claim, the authors also analyzed attenuated total reflection surface-enhanced infrared absorption spectroscopy (ATR-SEIRA) during EGOR at 0.5 V (vs. RHE) (Figure 9e,f). First, the intensity of CO_2 signals at 2343 cm^{-1} for 0.4% Mo-doped Pt_3Mn is higher than Pt_3Mn, revealing better EGOR performance. The authors have collected CO_2 after 35 s, and the amount per unit catalyst surface area is nearly two times higher for the 0.4% Mo-doped Pt_3Mn catalyst than Pt_3Mn catalyst. Secondly, the CO_L band at 2050 cm^{-1} broadens at Pt_3Mn surface with time, while the band is suppressed on the 0.4% Mo-doped Pt3Mn surface. Therefore, Mo doping inhibits CO_L species formation and acts as anti-CO sites on Pt_3Mn surface.

Interestingly, authors have analyzed CV curves of Pt_3Mn and 4% Mn-doped Pt_3Mn after the chronoamperometric test (Figure 9g,h) and correlated the voltammetric profile peaks with surface structure evolution. During the first cycle, the hydrogen adsorption/desorption peaks were weaker, and two apparent peaks at 0.11 and 0.24 V belong to (110) and (100) facets, respectively. For Pt_3Mn catalyst (Figure 9g), the (100) peak (terrace) exhibits a rapid downtrend with time, compared with the (110) peak (step). This phenomenon may originate from the fact that in bimetallic Pt nanocrystals, Pt atoms tend to be located on peaks and edges while transition metal atoms occupy the crystal facet [124]. On the contrary, 4% Mn-doped Pt_3Mn showed a gentler downtrend with time for the peaks related to (110) and (100) facets (Figure 9h). Also, at 0.7 V, Pt_3Mn shows a shift in onset potential for OH adsorption with time, signifying the leaching of Mn from the Pt surface. But, on the 4% Mn-doped Pt_3Mn, the slight changes reveal that doped Mo can stabilize Pt_3Mn during the stability test. To further confirm the stabilizing effect, the authors have conducted DFT calculations on different Mo-doped surfaces (Figure 9i). When Mo was doped on Pt_3Mn alloy, the binding energy of Pt changed from 5.82 to 5.84 eV (Mo doping on the surface) or 5.71 eV (Mo doping on the subsurface), while the binding energy of Mn changed from 5.14 to 6.49 eV (Mo doping on the surface) or 6.30 eV (Mo doping on the subsurface). Based on the binding energy, the authors expressed that Mo doping on Pt_3Mn creates strongly bonded Mo-Mn instead of Pt-Mn and Pt-Mo bonds, and this phenomenon leads to the anti-dissolution of Mn during EGOR.

In a similar study by Wang et al., Bi-decorated Pd concave nanocubes (CNCs) exhibited improved EGOR performance by following the C1 pathway compared to bare Pd CNCs in a 1 M NaOH + 1 M EG solution [133]. The Bi-decorated Pd CNC showed an increased specific activity of 2.44 times compared to the Pd CNC electrode toward EGOR in alkaline media. Earlier, OH_{ad} was regarded as a reactive pair in the LFOR in alkaline media [134,135]. Therefore, the promoted EGOR on Bi-decorated Pd CNCs may be ascribed to the modification of the electronic state of Pd by oxophilic Bi adatoms, assisting in the formation of OH_{ads}. Finally, the bifunctional mechanism is followed for eliminating CO_{ads} species to CO_2. However, the authors also pointed out that the formation of adsorbed CO_{ads} during the EGOR should not be simply defined as a poisoning species rather than an active intermediate to be converted to CO_2 (HCO_3^- and CO_3^{2-}) [136].

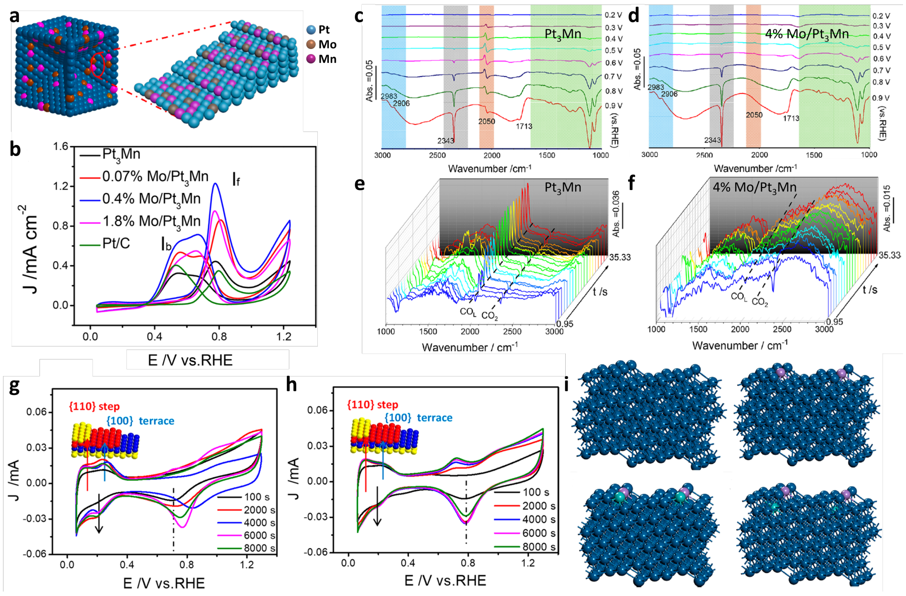

Figure 9. (**a**) Surface Illustration of the Mo-doped Pt_3Mn catalyst. (**b**) CV for EGOR of Pt_3Mn, 0.4% Mo-doped Pt_3Mn, and commercial Pt/C in 0.1 M $HClO_4$ + 0.5 M EG solution at a scan rate of 50 mV·s^{-1}. In-situ FTIR spectra for EGOR on (**c**) Pt_3Mn and (**d**) 0.4% Mo-doped Pt_3Mn catalyst in 0.1 M $HClO_4$ + 0.5 M EG solution. Real-time ATR-SEIRA spectra of (**e**) Pt_3Mn and (**f**) 0.4% Mo-doped Pt_3Mn catalyst in 0.1 M $HClO_4$ + 0.5 M EG solution at 500 mV vs. RHE (temporal resolution 0.95 s/spectrum). CV curves of (**g**) Pt_3Mn and (**h**) 0.4% Mo-doped Pt_3Mn after different chronoamperometric tests. (**i**) Geometrical structures of Pt (410) surface (**left top**), Pt_3Mn step edge (**right top**), surface Mo-doped Pt_3Mn step edge (**left bottom**), subsurface Mo-doped Pt_3Mn step edge (**right bottom**). The indigo, purple, and grass green balls denote the Pt, Mn, and Mo atoms, respectively. Reproduced with permission [124]. Copyright 2019, American Chemical Society.

Interestingly, Ir decoration on Pd nanosheet can also lead to higher EGOR performance, which was discussed by Wang et al. [137]. The introduction of Ir as a dopant into the Pd surface can effectively reform the Pd–Pd bond, favoring the downshift of the d-band center. These led to the faster adsorption of H_2O, and CO_{ads} was removed easily from the surface during EGOR. An overall comparison of the EGOR performance of various decorated nanocatalysts is shown in Table 5.

Table 5. Comparison of the EGOR performance of various decorated nanocatalysts.

Catalyst	MA [a] ($A\cdot mg_{Pt/Pd}^{-1}$)	MA Enhancement vs. Pt/C or Pd/C	SA [b] ($mA\cdot cm^{-2}$)	SA Enhancement vs. Pt/C or Pd/C	CA Stability [c]	Electrolyte	Ref.
Mo doped Pt_3Mn	0.23	~2	1.23	~3	~20% specific activity retention after 2000 s	0.5 M $(CH_2OH)_2$ + 0.1 M $HClO_4$	[124]
Bi decorated Pd CNC	N/A	N/A	N/A	~2.44 (apparent SA vs. Pd CNC)	N/A	1.0 M $(CH_2OH)_2$ + 1.0 M NaOH	[133]
Ir doped Pd NSAs	4.32	3.64 (vs. Pd/C)	3.29	2.78 (vs. Pd/C)	~30% mass activity retention after 4000 s	1.0 M $(CH_2OH)_2$ + 1.0 M KOH	[137]
Pt_3Mn–Ru CNCs	0.24	2.05	1.32	3.77	N/A	0.5 M $(CH_2OH)_2$ + 0.1 M $HClO_4$	[138]
Se doped Pd-PdSe HNSs	8.60	6.6	15.7	5.5	~60% mass activity retention after 5000 s	1.0 M $(CH_2OH)_2$ + 1.0 M KOH	[139]
Au-Doped PtBi	28.72	8.65	N/A	N/A	~20% mass activity retention after 3600 s	0.5 M $(CH_2OH)_2$ + 1.0 M KOH	[140]

[a] Mass activity, [b] Specific activity, [c] Chronoamperometry.

Surface decoration significantly enhances EGOR by weakening C–C bond in EG, stabilizing high-index facets, and suppressing strongly adsorbed CO-like species. Studies demonstrate that dopant placement can shift the mechanism toward direct oxidation with minimal poisoning. Nonetheless, the structural evolution of decorated surfaces under EGOR conditions-especially dissolution or migration of dopants remains an unresolved challenge. In this view, designing dopants that anchor strongly to step/kink sites and resist leaching will be the key to overcome EGOR. Future work should also combine DFT insights with real-time spectroscopic tracking to fully understand the mechanism between dopant distribution, surface reconstruction, and EGOR pathway selectivity.

5. Conclusions and Outlook

We have summarized synthesis protocols and outlined the properties of anti-CO sites affecting the LFOR of catalysts to achieve maximum performance. The indirect pathway or failure to split the C–C bond in liquid fuel will result in CO adsorption on the catalytic surface. Continuous Pt or Pd sites are more favorable for bridge CO_{ads}, which require more energy to free the catalyst surface from CO_{ads}. As discussed in this review, this phenomenon can be minimized by decorating the Pt surface with metal dopants. To date, synthetic strategies have made impressive progress in decorating noble metal and non-noble metal catalysts for efficient LFOR. Figure 10 delivers an overview of the reported metal dopants for decorating Pt or Pd surface utilized for LFOR. The scientific community is still investigating LFOR performance enhancement for the vast commercialization of DLFCs.

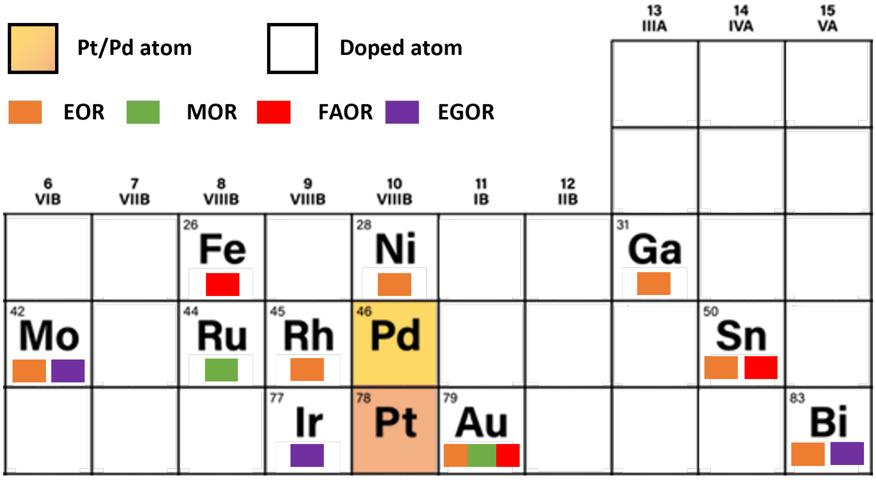

Figure 10. Overview of reported metal dopants for decorating Pt or Pd surface utilized for various LFOR.

To provide insight into the influential roles of those anti-CO sites on LFOR, we have compared all the catalysts that have been reported so far. As the experimental operation conditions are different for each study, one way to compare nanocatalysts is in terms of the shift in the onset of the CO stripping experiment versus mass activity enhancement compared to commercial Pt/C. It is evident that the more the deviation from the CO stripping onset compared to Pt/C, the better the LFOR performance of the catalyst. Although a decorated nanocatalyst has shown improved LFOR performance, many challenges remain to be addressed regarding (i) synthesis, (ii) optimization of catalytic performance, (iii) dissolution of metal during electrocatalysis, and (iv) combination of theoretical and experimental approaches to further understand the reaction mechanisms. As an outlook for the field, we highlight a few crucial challenges for further developing decorated nanocatalysts toward LFOR.

(i) *Easier regeneration of active sites after stability test.* Catalyst deactivation is the most common and consistent issue for LFOR. This review shows that the deactivation of catalysts during LFOR stability performance can be minimized by decorating the catalyst's surface, but cannot be eliminated entirely. CO can still be adsorbed on the decorated surface and deteriorate the electrocatalytic performance over time, as seen in every chronoamperometric stability test. Therefore, a catalyst with easier regeneration of active sites may address the problem. For example, $Bi(OH)_2$ decorated PdBi showed that the active anti-CO species could be regenerated easily on cycling in 1M NaOH solution while retaining its activity. Therefore, developing such nanocatalysts for long-term LFOR performance is desirable.

(ii) *Multi-metallic surface decoration.* The anti-CO poisoning effect can be enhanced by decorating three or more transition metals on the noble metal surface. For example, Rh and Sn decorated Pt toward EOR, Au decorated PtFe, Fe-doped PtRu NWs for FAOR, and Mo-doped Pt_3Mn for EGOR have been investigated. Interestingly, these catalysts showed superior electrocatalytic performance than commercial Pt/C. Therefore, it is an endless possibility to explore different decorated structures suitable for LFOR. Of course, the theoretical analysis would reveal if the catalyst is ideal for breaking C–C bonds of liquid fuels and the reaction pathways before practical research is conducted.

(iii) *Synthesis protocol.* Although hundreds of studies are pouring in for bimetallic surface synthesis toward LFOR, only a few are good enough to design and tailor electrocatalysts with a preferentially decorated structure. That is to say, that synthesis may have resulted in a decorated surface, but if there is too much active site coverage by anti-CO sites, it may interrupt the whole reaction, as reactants will not adsorb on the catalyst surface. Therefore, the degree of decoration or optimal surface composition must be considered when decorating the catalytic surface with dopants.

(iv) *Robust analytical techniques for the determination of roles of anti-CO-sites.* With current cutting-edge technology, it is possible to identify the doped/decorated metal using XPS, ICP-AES, HRTEM, and EDX analysis. However, detecting the decorated metal acting as an anti-CO poisoning species would be interesting to analyze and report. Few studies reported in-situ FTIR analysis during LFOR, but the metal oxidation state was unknown during the reaction. In-situ XAS, which has often been used to reveal the structural changes (including the metal oxidation state, bond distances, and coordination numbers) and their dependence on potential, might also become a powerful tool in disclosing the role of decorated metal as anti-CO poisoning sites for improved activity and stability.

Author Contributions: M.K.K.: Conceptualization, writing—original draft preparation. J.K.: Conceptualization, writing—original draft preparation. S.S.: Writing—reviewing. S.-I.C.: Conceptualization, supervision, writing—reviewing, and editing. All authors have read and agreed to the published version of the manuscript.

Funding: This study was supported by the National Research Foundation of Korea (RS-2024-00346153, RS-2025-02215028).

Data Availability Statement: Not applicable.

Conflicts of Interest: The authors declare no conflict of interest.

Use of AI and AI-Assisted Technologies: No AI tools were utilized for this paper.

References

1. Cheng, H.; Wang, J.; Wu, C.; Liu, Z. Electrocatalysts for Formic Acid-Powered PEM Fuel Cells: Challenges and Prospects. *Energy Mater. Adv.* **2025**, *4*, 67.
2. Chang, J.; Wang, G.; Zhang, W.; Yang, Y. Atomically Dispersed Catalysts for Small Molecule Electrooxidation in Direct Liquid Fuel Cells. *J. Energy Chem.* **2022**, *68*, 439–453.
3. Ramli, Z.A.C.; Pasupuleti, J.; Samidin, S.; Saharuddin, T.S.T.; Isahak, W.N.R.W.; Sofiah, A.G.N.; Koh, S.P.; Kiong, S.T. Recent Advances of Two-Dimensional-Based (2D) Materials as Electrocatalysts in DLFC: An Overview. *Fuel* **2025**, *387*, 134386.

4. Li, Y.; Yao, M.-S.; He, Y.; Du, S. Recent Advances of Electrocatalysts and Electrodes for Direct Formic Acid Fuel Cells: From Nano to Meter Scale Challenges. *Nano-Micro Lett.* **2025**, *17*, 148.
5. Shaari, N.; Kamarudin, S.K.; Bahru, R.; Osman, S.H.; Md Ishak, N.A.I. Progress and Challenges: Review for Direct Liquid Fuel Cell. *Int. J. Energy Res.* **2021**, *45*, 6644–6688.
6. Altarawneh, R.M. Overview on the Vital Step toward Addressing Platinum Catalyst Poisoning Mechanisms in Acid Media of Direct Ethanol Fuel Cells (DEFCs). *Energy Fuels* **2021**, *35*, 11594–11612.
7. Cai, B.; Chen, X.; Wang, L.; Fu, H. Advanced Progress for Promoting Anodic Hydrogen Oxidation Activity and Anti-CO Poisoning in Fuel Cells. *ACS Catal.* **2024**, *14*, 13602–13629.
8. Chen, A.; Ostrom, C. Palladium-Based Nanomaterials: Synthesis and Electrochemical Applications. *Chem. Rev.* **2015**, *115*, 11999–12044.
9. Kabiraz, M.K.; Kim, J.; Lee, W.-J.; Ruqia, B.; Kim, H.C.; Lee, S.-U.; Kim, J.-R.; Paek, S.-M.; Hong, J.W.; Choi, S.-I. Ligand Effect of Shape-Controlled β-Palladium Hydride Nanocrystals on Liquid-Fuel Oxidation Reactions. *Chem. Mater.* **2019**, *31*, 5663–5673.
10. Antolini, E. Palladium in Fuel Cell Catalysis. *Energy Environ. Sci.* **2009**, *2*, 915–931.
11. Zhang, H.; Jin, M.; Xia, Y. Enhancing the Catalytic and Electrocatalytic Properties of Pt-Based Catalysts by Forming Bimetallic Nanocrystals with Pd. *Chem. Soc. Rev.* **2012**, *41*, 8035–8049.
12. Wu, C.; Zhang, Y.; Yang, H.Y. Rational Design and Facile Preparation of Palladium-Based Electrocatalysts for Small Molecules Oxidation. *ChemSusChem* **2025**, *18*, e202401127.
13. Neto, A.O.; Dias, R.R.; Tusi, M.M.; Linardi, M.; Spinacé, E.V. Electro-Oxidation of Methanol and Ethanol Using PtRu/C, PtSn/C and PtSnRu/C Electrocatalysts Prepared by an Alcohol-Reduction Process. *J. Power Sources* **2007**, *166*, 87–91.
14. Busó-Rogero, C.; Herrero, E.; Feliu, J.M. Ethanol Oxidation on Pt Single-Crystal Electrodes: Surface-Structure Effects in Alkaline Medium. *ChemPhysChem* **2014**, *15*, 2019–2028.
15. Ozoemena, K.I. Nanostructured Platinum-Free Electrocatalysts in Alkaline Direct Alcohol Fuel Cells: Catalyst Design, Principles and Applications. *RSC Adv.* **2016**, *6*, 89523–89550.
16. Liao, Y.; Chen, W.; Ding, Y.; Xie, L.; Yang, Q.; Wu, Q.; Liu, X.; Zhu, J.; Feng, R.; Fu, X.-Z. Boosting Alcohol Oxidation Electrocatalysis with Multifactorial Engineered Pd1/Pt Single-Atom Alloy-BiOx Adatoms Surface. *Nano-Micro Lett.* **2025**, *17*, 172.
17. Mai, Q.; Mai, Y.; Zhong, Y.; Xue, R.; Jia, B.; Guan, X.; Du, W.; Pan, H.; Li, Y.; Zhang, Z. Intermetallic Electrocatalysts for Small-Molecule Fuel Oxidation. *Adv. Energy Mater.* **2025**, *15*, 2500415.
18. Kwon, T.; Kim, T.; Son, Y.; Lee, K. Dopants in the Design of Noble Metal Nanoparticle Electrocatalysts and Their Effect on Surface Energy and Coordination Chemistry at the Nanocrystal Surface. *Adv. Energy Mater.* **2021**, *11*, 2100265.
19. Chen, Q.-S.; Vidal-Iglesias, F.J.; Solla-Gullón, J.; Sun, S.-G.; Feliu, J.M. Role of Surface Defect Sites: From Pt Model Surfaces to Shape-Controlled Nanoparticles. *Chem. Sci.* **2012**, *3*, 136–147.
20. Bommersbach, P.; Chaker, M.; Mohamedi, M.; Guay, D. Physico-Chemical and Electrochemical Properties of Platinum−Tin Nanoparticles Synthesized by Pulsed Laser Ablation for Ethanol Oxidation. *J. Phys. Chem. C* **2008**, *112*, 14672–14681.
21. Hsieh, C.-T.; Lin, J.-Y. Fabrication of Bimetallic Pt–M (M=Fe, Co, and Ni) Nanoparticle/Carbon Nanotube Electrocatalysts for Direct Methanol Fuel Cells. *J. Power Sources* **2009**, *188*, 347–352.
22. Kowal, A.; Li, M.; Shao, M.; Sasaki, K.; Vukmirovic, M.B.; Zhang, J.; Marinkovic, N.S.; Liu, P.; Frenkel, A.I.; Adzic, R.R. Ternary Pt/Rh/SnO_2 Electrocatalysts for Oxidizing Ethanol to CO_2. *Nat. Mater.* **2009**, *8*, 325–330.
23. Koper, M.T.M. Structure Sensitivity and Nanoscale Effects in Electrocatalysis. *Nanoscale* **2011**, *3*, 2054–2073.
24. Erini, N.; Rudi, S.; Beermann, V.; Krause, P.; Yang, R.; Huang, Y.; Strasser, P. Exceptional Activity of a Pt–Rh–Ni Ternary Nanostructured Catalyst for the Electrochemical Oxidation of Ethanol. *ChemElectroChem* **2015**, *2*, 903–908.
25. Ong, B.C.; Kamarudin, S.K.; Basri, S. Direct Liquid Fuel Cells: A Review. *Int. J. Hydrogen Energy* **2017**, *42*, 10142–10157.
26. Karim, N.A.; Kamarudin, S.K. *Chapter 2—Introduction to Direct Alcohol Fuel Cells (DAFCs)*; Akay, R.G., Akay, R.G., Yurtcan, A.B., Eds.; Academic Press: London, UK, 2021; pp. 49–70.
27. Ponmani, K.; Durga, S.; Arun, A.; Kiruthika, S.; Muthukumaran, B. Development of Membraneless Sodium Perborate Fuel Cell for Media Flexible Power Generation. *Int. J. Electrochem.* **2014**, *2014*, 962161.
28. Arenz, M.; Mayrhofer, K.J.J.; Stamenkovic, V.; Blizanac, B.B.; Tomoyuki, T.; Ross, P.N.; Markovic, N.M. The Effect of the Particle Size on the Kinetics of CO Electrooxidation on High Surface Area Pt Catalysts. *J. Am. Chem. Soc.* **2005**, *127*, 6819–6829.
29. Li, X.; Haunold, T.; Werkovits, S.; Marks, L.D.; Blaha, P.; Rupprechter, G. CO Adsorption and Disproportionation on Smooth and Defect-Rich Ir(111). *J. Phys. Chem. C* **2022**, *126*, 6578–6589.
30. Fang, Q.; Zhang, Z.; Yang, X.; Cheng, T.; Ma, X.; Tang, J. Cu_2O Nanoparticles with Controlled Surface Roughness for CO_2 Electroreduction towards C_{2+} Products. *Chem. Eng. J.* **2025**, *515*, 163293.
31. Cao, L.; Soto, F.A.; Li, D.; Deng, T.; Hu, E.; Lu, X.; Cullen, D.A.; Eidson, N.; Yang, X.-Q.; He, K.; et al. Pd-Ru Pair on Pt Surface for Promoting Hydrogen Oxidation and Evolution in Alkaline Media. *Nat. Commun.* **2024**, *15*, 7245.

32. Long, D.; Liu, Y.; Ping, X.; Chen, F.; Tao, X.; Xie, Z.; Wang, M.; Wang, M.; Li, L.; Guo, L.; et al. Constructing CO-Immune Water Dissociation Sites around Pt to Achieve Stable Operation in High CO Concentration Environment. *Nat. Commun.* **2024**, *15*, 8105.
33. Huang, H.; Hayes, E.T.C.; Gianolio, D.; Cibin, G.; Hage, F.S.; Ramasse, Q.M.; Russell, A.E. Role of SnO2 in the Bifunctional Mechanism of CO Oxidation at Pt-SnO_2 Electrocatalysts. *ChemElectroChem* **2021**, *8*, 2572–2582.
34. Berretti, E.; Osmieri, L.; Baglio, V.; Miller, H.A.; Filippi, J.; Vizza, F.; Santamaria, M.; Specchia, S.; Santoro, C.; Lavacchi, A. Direct Alcohol Fuel Cells: A Comparative Review of Acidic and Alkaline Systems. *Electrochem. Energy Rev.* **2023**, *6*, 30.
35. Li, M.; Adzic, R.R. *Low-Platinum-Content Electrocatalysts for Methanol and Ethanol Electrooxidation BT—Electrocatalysis in Fuel Cells: A Non- and Low-Platinum Approach*; Shao, M., Ed.; Springer: London, UK, 2013; pp. 1–25.
36. Wang, Y.; Zou, S.; Cai, W.-B. Recent Advances on Electro-Oxidation of Ethanol on Pt- and Pd-Based Catalysts: From Reaction Mechanisms to Catalytic Materials. *Catalysts* **2015**, *5*, 1507–1534.
37. Flórez-Montaño, J.; García, G.; Guillén-Villafuerte, O.; Rodríguez, J.L.; Planes, G.A.; Pastor, E. Mechanism of Ethanol Electrooxidation on Mesoporous Pt Electrode in Acidic Medium Studied by a Novel Electrochemical Mass Spectrometry Set-Up. *Electrochim. Acta* **2016**, *209*, 121–131.
38. Dai, L.-X.; Wang, X.-Y.; Yang, S.-S.; Zhang, T.; Ren, P.-J.; Ye, J.-Y.; Nan, B.; Wen, X.-D.; Zhou, Z.-Y.; Si, R.; et al. Intrinsic Composition and Electronic Effects of Multicomponent Platinum Nanocatalysts with High Activity and Selectivity for Ethanol Oxidation Reaction. *J. Mater. Chem. A* **2018**, *6*, 11270–11280.
39. Asiri, H.A.; Anderson, A.B. Mechanisms for Ethanol Electrooxidation on Pt(111) and Adsorption Bond Strengths Defining an Ideal Catalyst. *J. Electrochem. Soc.* **2015**, *162*, F115.
40. Yang, Y.-Y.; Ren, J.; Li, Q.-X.; Zhou, Z.-Y.; Sun, S.-G.; Cai, W.-B. Electrocatalysis of Ethanol on a Pd Electrode in Alkaline Media: An in Situ Attenuated Total Reflection Surface-Enhanced Infrared Absorption Spectroscopy Study. *ACS Catal.* **2014**, *4*, 798–803.
41. Chang, Q.; Hong, Y.; Lee, H.J.; Lee, J.H.; Ologunagba, D.; Liang, Z.; Kim, J.; Kim, M.J.; Hong, J.W.; Song, L.; et al. Achieving Complete Electrooxidation of Ethanol by Single Atomic Rh Decoration of Pt Nanocubes. *Proc. Natl. Acad. Sci. USA* **2022**, *119*, e2112109119.
42. Schnaidt, J.; Heinen, M.; Jusys, Z.; Behm, R.J. Mechanistic Aspects of the Electro-Oxidation of Ethylene Glycol on a Pt-Film Electrode: A Combined in Situ IR Spectroscopy and Online Mass Spectrometry Study of Kinetic Isotope Effects. *Catal. Today* **2013**, *202*, 154–162.
43. Liu, Y.; Hu, P.; Wei, M.; Wang, C. Electrocatalytic Study of Ethylene Glycol Oxidation on Pt3Sn Alloy Nanoparticles. *ChemElectroChem* **2019**, *6*, 1004–1008.
44. Kabiraz, M.K.; Wahidah, H.; Hong, J.W.; Choi, S.-I. Platinum Metallenes: Advanced Electrocatalysts for Sustainable Energy Solutions. *Small* **2025**, *21*, 2500858.
45. Tong, Y.; Yan, X.; Liang, J.; Dou, S.X. Metal-Based Electrocatalysts for Methanol Electro-Oxidation: Progress, Opportunities, and Challenges. *Small* **2021**, *17*, 1904126.
46. Ayán-Varela, M.; Ruiz-Rosas, R.; Villar-Rodil, S.; Paredes, J.I.; Cazorla-Amorós, D.; Morallón, E.; Martínez-Alonso, A.; Tascón, J.M.D. Efficient Pt Electrocatalysts Supported onto Flavin Mononucleotide-Exfoliated Pristine Graphene for the Methanol Oxidation Reaction. *Electrochim. Acta* **2017**, *231*, 386–395.
47. Mu, Y.; Liang, H.; Hu, J.; Jiang, L.; Wan, L. Controllable Pt Nanoparticle Deposition on Carbon Nanotubes as an Anode Catalyst for Direct Methanol Fuel Cells. *J. Phys. Chem. B* **2005**, *109*, 22212–22216.
48. Watanabe, M.; Motoo, S. Electrocatalysis by Ad-Atoms: Part III. Enhancement of the Oxidation of Carbon Monoxide on Platinum by Ruthenium Ad-Atoms. *J. Electroanal. Chem. Interfacial Electrochem.* **1975**, *60*, 275–283.
49. Pei, A.; Ruan, L.; Liu, B.; Chen, W.; Lin, S.; Chen, B.; Liu, Y.; Zhu, L.H.; Chen, B.H. Ultra-Low Au Decorated PtNi Alloy Nanoparticles on Carbon for High-Efficiency Electro-Oxidation of Methanol and Formic Acid. *Int. J. Hydrogen Energy* **2020**, *45*, 22893–22905.
50. Bhalothia, D.; Huang, T.-H.; Chou, P.-H.; Wang, K.-W.; Chen, T.-Y. Promoting Formic Acid Oxidation Performance of Pd Nanoparticles via Pt and Ru Atom Mediated Surface Engineering. *RSC Adv.* **2020**, *10*, 17302–17310.
51. Bhalothia, D.; Huang, T.-H.; Chou, P.-H.; Chen, P.-C.; Wang, K.-W.; Chen, T.-Y. CO-Reductive and O_2-Oxidative Annealing Assisted Surface Restructure and Corresponding Formic Acid Oxidation Performance of PdPt and PdRuPt Nanocatalysts. *Sci. Rep.* **2020**, *10*, 8457.
52. Xia, S.; Wu, F.; Liu, Q.; Gao, W.; Guo, C.; Wei, H.; Hussain, A.; Zhang, Y.; Xu, G.; Niu, W. Steering the Selective Production of Glycolic Acid by Electrocatalytic Oxidation of Ethylene Glycol with Nanoengineered PdBi-Based Heterodimers. *Small* **2024**, *20*, 2400939.
53. Schnaidt, J.; Heinen, M.; Jusys, Z.; Behm, R.J. Oxidation of the Partly Oxidized Ethylene Glycol Oxidation Products Glycolaldehyde, Glyoxal, Glycolic Acid, Glyoxylic Acid, and Oxalic Acid on Pt Electrodes: A Combined ATR-FTIRS and DEMS Spectroelectrochemical Study. *J. Phys. Chem. C* **2013**, *117*, 12689–12701.

54. Yue, H.; Zhao, Y.; Ma, X.; Gong, J. Ethylene Glycol: Properties, Synthesis, and Applications. *Chem. Soc. Rev.* **2012**, *41*, 4218–4244.
55. Zhong, J.; Bin, D.; Feng, Y.; Zhang, K.; Wang, J.; Wang, C.; Guo, J.; Yang, P.; Du, Y. Synthesis and High Electrocatalytic Activity of Au-Decorated Pd Heterogeneous Nanocube Catalysts for Ethanol Electro-Oxidation in Alkaline Media. *Catal. Sci. Technol.* **2016**, *6*, 5397–5404.
56. Yuan, X.; Zhang, Y.; Cao, M.; Zhou, T.; Jiang, X.; Chen, J.; Lyu, F.; Xu, Y.; Luo, J.; Zhang, Q.; et al. $Bi(OH)_3$/PdBi Composite Nanochains as Highly Active and Durable Electrocatalysts for Ethanol Oxidation. *Nano Lett.* **2019**, *19*, 4752–4759.
57. Gao, L.; Yang, Z.; Sun, T.; Tan, X.; Lai, W.; Li, M.; Kim, J.; Lu, Y.-F.; Choi, S.-I.; Zhang, W.; et al. Autocatalytic Surface Reduction-Assisted Synthesis of PtW Ultrathin Alloy Nanowires for Highly Efficient Hydrogen Evolution Reaction. *Adv. Energy Mater.* **2022**, *12*, 2103943.
58. Wasmus, S.; Küver, A. Methanol Oxidation and Direct Methanol Fuel Cells: A Selective Review. *J. Electroanal. Chem.* **1999**, *461*, 14–31.
59. Tiwari, J.N.; Tiwari, R.N.; Singh, G.; Kim, K.S. Recent Progress in the Development of Anode and Cathode Catalysts for Direct Methanol Fuel Cells. *Nano Energy* **2013**, *2*, 553–578.
60. Park, J.; Kwon, T.; Kim, J.; Jin, H.; Kim, H.Y.; Kim, B.; Joo, S.H.; Lee, K. Hollow Nanoparticles as Emerging Electrocatalysts for Renewable Energy Conversion Reactions. *Chem. Soc. Rev.* **2018**, *47*, 8173–8202.
61. Aricò, A.S.; Srinivasan, S.; Antonucci, V. DMFCs: From Fundamental Aspects to Technology Development. *Fuel Cells* **2001**, *1*, 133–161.
62. Yuda, A.; Ashok, A.; Kumar, A. A Comprehensive and Critical Review on Recent Progress in Anode Catalyst for Methanol Oxidation Reaction. *Catal. Rev.* **2022**, *64*, 126–228.
63. Liu, M.; Zhang, Z.; Li, C.; Jin, S.; Zhu, K.; Fan, S.; Li, J.; Liu, K. High-Entropy Alloyed Single-Atom Pt for Methanol Oxidation Electrocatalysis. *Nat. Commun.* **2025**, *16*, 6359.
64. Li, P.; Hu, Q.; Fan, W.; Li, M.; Zhou, C.; Zhang, H.; Chen, L.; Pan, Z.; Jiao, X.; Chen, Q. Synergistic Multi-Active Sites in High-Entropy Alloy Nanowires Enhances the Methanol Oxidation Reaction Performances. *Small* **2025**, *21*, 2506472.
65. Xing, S.; Liu, Z.; Jiang, Y.; Tang, P.; Zhang, J.; Chen, J.; Li, H.; Li, C. Platinum-Copper Nanowire Networks with Enhanced CO Tolerance toward Methanol Oxidation Electrocatalysis. *Chem. Sci.* **2025**, *16*, 9311–9319
66. Lin, Z.; Chen, W.; Jiang, Y.; Bian, T.; Zhang, H.; Wu, J.; Wang, Y.; Yang, D. Facile Synthesis of Ru-Decorated Pt Cubes and Icosahedra as Highly Active Electrocatalysts for Methanol Oxidation. *Nanoscale* **2016**, *8*, 12812–12818.
67. Maiyalagan, T.; Alaje, T.O.; Scott, K. Highly Stable Pt–Ru Nanoparticles Supported on Three-Dimensional Cubic Ordered Mesoporous Carbon (Pt–Ru/CMK-8) as Promising Electrocatalysts for Methanol Oxidation. *J. Phys. Chem. C* **2012**, *116*, 2630–2638.
68. Takeguchi, T.; Yamanaka, T.; Asakura, K.; Muhamad, E.N.; Uosaki, K.; Ueda, W. Evidence of Nonelectrochemical Shift Reaction on a CO-Tolerant High-Entropy State Pt–Ru Anode Catalyst for Reliable and Efficient Residential Fuel Cell Systems. *J. Am. Chem. Soc.* **2012**, *134*, 14508–14512.
69. Nilekar, A.U.; Sasaki, K.; Farberow, C.A.; Adzic, R.R.; Mavrikakis, M. Mixed-Metal Pt Monolayer Electrocatalysts with Improved CO Tolerance. *J. Am. Chem. Soc.* **2011**, *133*, 18574–18576.
70. Gasteiger, H.A.; Markovic, N.; Ross, P.N.; Cairns, E.J. Methanol Electrooxidation on Well-Characterized Platinum-Ruthenium Bulk Alloys. *J. Phys. Chem.* **1993**, *97*, 12020–12029.
71. Zhao, X.; Yin, M.; Ma, L.; Liang, L.; Liu, C.; Liao, J.; Lu, T.; Xing, W. Recent Advances in Catalysts for Direct Methanol Fuel Cells. *Energy Environ. Sci.* **2011**, *4*, 2736–2753.
72. Yajima, T.; Wakabayashi, N.; Uchida, H.; Watanabe, M. Adsorbed Water for the Electro-Oxidation of Methanol at Pt–Ru Alloy. *Chem. Commun.* **2003**, *7*, 828–829.
73. Pelliccione, C.J.; Timofeeva, E.V.; Katsoudas, J.P.; Segre, C.U. In Situ Ru K-Edge X-Ray Absorption Spectroscopy Study of Methanol Oxidation Mechanisms on Model Submonolayer Ru on Pt Nanoparticle Electrocatalyst. *J. Phys. Chem. C* **2013**, *117*, 18904–18912.
74. Cai, Z.; Lu, Z.; Bi, Y.; Li, Y.; Kuang, Y.; Sun, X. Superior Anti-CO Poisoning Capability: Au-Decorated PtFe Nanocatalysts for High-Performance Methanol Oxidation. *Chem. Commun.* **2016**, *52*, 3903–3906.
75. Gu, J.; Liu, W.-C.; Zhao, Z.-Q.; Lan, G.-X.; Zhu, W.; Zhang, Y.-W. Pt/Ru/C Nanocomposites for Methanol Electrooxidation: How Ru Nanocrystals' Surface Structure Affects Catalytic Performance of Deposited Pt Particles. *Inorg. Chem. Front.* **2014**, *1*, 109–117.
76. Freitas, R.G.; Marchesi, L.F.Q.; Forim, M.R.; Bulhões, L.O.; Pereira, E.C.; Santos, M.C.; Oliveira, R.T. Ethanol Electrooxidation Using $Ti/(RuO_2)_{(x)}Pt_{(1-x)}$ Electrodes Prepared by the Polymeric Precursor Method. *J. Braz. Chem. Soc.* **2011**, *22*, 1709–1717.
77. Freitas, R.G.; Marchesi, L.F.; Oliveira, R.T.S.; Mattos-Costa, F.I.; Pereira, E.C.; Bulhoes, L.O.S.; Santos, M.C. Methanol Oxidation Reaction on $Ti/(RuO_2)_{(x)}Pt_{(1-x)}$ Electrodes Prepared by the Polymeric Precursor Method. *J. Power Sources* **2007**, *171*, 373–380.

78. Park, J.; Kim, H.J.; Oh, A.; Kwon, T.; Baik, H.; Choi, S.-I.; Lee, K. RuO X-Decorated Multimetallic Hetero-Nanocages as Highly Efficient Electrocatalysts toward the Methanol Oxidation Reaction. *Nanoscale* **2018**, *10*, 21178–21185.
79. Qiao, B.; Wang, A.; Yang, X.; Allard, L.F.; Jiang, Z.; Cui, Y.; Liu, J.; Li, J.; Zhang, T. Single-Atom Catalysis of CO Oxidation Using Pt_1/FeO_X. *Nat. Chem.* **2011**, *3*, 634–641.
80. Fu, Q.; Li, W.-X.; Yao, Y.; Liu, H.; Su, H.-Y.; Ma, D.; Gu, X.-K.; Chen, L.; Wang, Z.; Zhang, H. Interface-Confined Ferrous Centers for Catalytic Oxidation. *Science* **2010**, *328*, 1141–1144.
81. Pedersen, M.Ø.; Helveg, S.; Ruban, A.; Stensgaard, I.; Lægsgaard, E.; Nørskov, J.K.; Besenbacher, F. How a Gold Substrate Can Increase the Reactivity of a Pt Overlayer. *Surf. Sci.* **1999**, *426*, 395–409.
82. Koenigsmann, C.; Semple, D.B.; Sutter, E.; Tobierre, S.E.; Wong, S.S. Ambient Synthesis of High-Quality Ruthenium Nanowires and the Morphology-Dependent Electrocatalytic Performance of Platinum-Decorated Ruthenium Nanowires and Nanoparticles in the Methanol Oxidation Reaction. *ACS Appl. Mater. Interfaces* **2013**, *5*, 5518–5530.
83. Marinkovic, N.S.; Li, M.; Adzic, R.R. Pt-based Catalysts for Electrochemical Oxidation of Ethanol. *Electrocatalysis* **2019**, *377*, 11.
84. Li, G.; Pickup, P.G. Analysis of Performance Losses of Direct Ethanol Fuel Cells with the Aid of a Reference Electrode. *J. Power Sources* **2006**, *161*, 256–263.
85. Xu, Y.; Zhang, B. Recent Advances in Porous Pt-Based Nanostructures: Synthesis and Electrochemical Applications. *Chem. Soc. Rev.* **2014**, *43*, 2439–2450.
86. Zhu, W.; Ke, J.; Wang, S.-B.; Ren, J.; Wang, H.-H.; Zhou, Z.-Y.; Si, R.; Zhang, Y.-W.; Yan, C.-H. Shaping Single-Crystalline Trimetallic Pt–Pd–Rh Nanocrystals toward High-Efficiency C–C Splitting of Ethanol in Conversion to CO_2. *ACS Catal.* **2015**, *5*, 1995–2008.
87. Kim, H.J.; Ruqia, B.; Kang, M.S.; Lim, S.B.; Choi, R.; Nam, K.M.; Seo, W.S.; Lee, G.; Choi, S.-I. Shape-Controlled Pt Nanocubes Directly Grown on Carbon Supports and Their Electrocatalytic Activity toward Methanol Oxidation. *Sci. Bull.* **2017**, *62*, 943–949.
88. Kim, K.S.; Hong, Y.; Kim, H.C.; Choi, S.; Hong, J.W. Ultrathin-Polyaniline-Coated Pt–Ni Alloy Nanooctahedra for the Electrochemical Methanol Oxidation Reaction. *Chem. Eur. J.* **2019**, *25*, 7185–7190.
89. Zhang, Z.; Liu, J.; Zhu, S.; Wang, Y.; Wang, J.; Xu, M.; Zhao, J.; Wang, Z.; Zeng, D.; Zeng, J. Dizygotic Atomic Platinum and Palladium on Carbon for High-Performance Ethanol and Methanol Electro-Oxidation. *Angew. Chem. Int. Ed.* **2025**, *64*, e202502348.
90. Kim, H.J.; Ahn, Y.-D.; Kim, J.; Kim, K.-S.; Jeong, Y.U.; Hong, J.W.; Choi, S.-I. Surface Elemental Distribution Effect of Pt-Pb Hexagonal Nanoplates for Electrocatalytic Methanol Oxidation Reaction. *Chin. J. Catal.* **2020**, *41*, 813–819.
91. Zhang, K.; Bin, D.; Yang, B.; Wang, C.; Ren, F.; Du, Y. Ru-Assisted Synthesis of Pd/Ru Nanodendrites with High Activity for Ethanol Electrooxidation. *Nanoscale* **2015**, *7*, 12445–12451.
92. Wu, Z.; Duan, R.; Cui, J.; Ye, C.; Zhang, S.; Yan, S. An Overview of the Pd Based Electrocatalysts Utilized in Direct Alcohol Fuel Cells. *Electrocatalysis* **2025**, *16*, 197–223.
93. Cui, Y.; Ma, K.; Chen, Z.; Yang, J.; Geng, Z.; Zeng, J. Atomic-Level Insights into Strain Effect on p-Nitrophenol Reduction via Au@Pd Core–Shell Nanocubes as an Ideal Platform. *J. Catal.* **2020**, *381*, 427–433.
94. Yuge, K.; Koyama, Y.; Kuwabara, A.; Tanaka, I. Surface Design of Alloy Protection against CO-Poisoning from First Principles. *J. Phys. Condens. Matter* **2014**, *26*, 355006.
95. Nguyen, M.T.X.; Nguyen, M.-K.; Pham, P.T.T.; Huynh, H.K.P.; Pham, H.H.; Vo, C.C.; Nguyen, S.T. High-Performance Pd-Coated Ni Nanowire Electrocatalysts for Alkaline Direct Ethanol Fuel Cells. *J. Electroanal. Chem.* **2021**, *888*, 115180.
96. Li, M.; Zhao, Z.; Xia, Z.; Yang, Y.; Luo, M.; Huang, Y.; Sun, Y.; Chao, Y.; Yang, W.; Yang, W.; et al. Lavender-Like Ga-Doped Pt3Co Nanowires for Highly Stable and Active Electrocatalysis. *ACS Catal.* **2020**, *10*, 3018–3026.
97. Mao, J.; Chen, W.; He, D.; Wan, J.; Pei, J.; Dong, J.; Wang, Y.; An, P.; Jin, Z.; Xing, W. Design of Ultrathin Pt-Mo-Ni Nanowire Catalysts for Ethanol Electrooxidation. *Sci. Adv.* **2017**, *3*, e1603068.
98. Hong, Y.; Kim, H.J.; Lee, H.J.; Kim, J.; Choi, S.-I. $Ni(OH)_2$ Decorated Pt–Cu Octahedra for Ethanol Electrooxidation Reaction. *Front. Chem.* **2019**, *7*, 608.
99. Fan, X.; Tang, M.; Wu, X.; Luo, S.; Chen, W.; Song, X.; Quan, Z. SnO_2 Patched Ultrathin PtRh Nanowires as Efficient Catalysts for Ethanol Electrooxidation. *J. Mater. Chem. A* **2019**, *7*, 27377–27382.
100. Gruzeł, G.; Szmuc, K.; Drzymała, E.; Piekarz, P.; Pajor-Świerzy, A.; Budziak, A.; Pastor, E. Thin Layer vs. Nanoparticles: Effect of SnO_2 Addition to PtRhNi Nanoframes for Ethanol Oxidation Reaction. *Int. J. Hydrogen Energy* **2022**, *47*, 14823–14835.
101. Yu, X.; Pickup, P.G. Recent Advances in Direct Formic Acid Fuel Cells (DFAFC). *J. Power Sources* **2008**, *182*, 124–132.
102. Rhee, Y.-W.; Ha, S.Y.; Masel, R.I. Crossover of Formic Acid through Nafion$^{®}$ Membranes. *J. Power Sources* **2003**, *117*, 35–38.
103. Demirci, U.B. Direct Liquid-Feed Fuel Cells: Thermodynamic and Environmental Concerns. *J. Power Sources* **2007**, *169*, 239–246.

104. Aslam, N.M.; Masdar, M.S.; Kamarudin, S.K.; Daud, W.R.W. Overview on Direct Formic Acid Fuel Cells (DFAFCs) as an Energy Sources. *Apcbee Procedia* **2012**, *3*, 33–39.
105. Capon, A.; Parson, R. The Oxidation of Formic Acid at Noble Metal Electrodes: I. Review of Previous Work. *J. Electroanal. Chem. Interfacial Electrochem.* **1973**, *44*, 1–7.
106. Capon, A.; Parsons, R. The Oxidation of Formic Acid on Noble Metal Electrodes: II. A Comparison of the Behaviour of Pure Electrodes. *J. Electroanal. Chem. Interfacial Electrochem.* **1973**, *44*, 239–254.
107. Fayette, M.; Nutariya, J.; Vasiljevic, N.; Dimitrov, N. A Study of Pt Dissolution during Formic Acid Oxidation. *Acs Catal.* **2013**, *3*, 1709–1718.
108. Rettenmaier, C.; Arán-Ais, R.M.; Timoshenko, J.; Rizo, R.; Jeon, H.S.; Kühl, S.; Chee, S.W.; Bergmann, A.; Roldan Cuenya, B. Enhanced Formic Acid Oxidation over SnO_2-Decorated Pd Nanocubes. *ACS Catal.* **2020**, *10*, 14540–14551.
109. Miyake, H.; Okada, T.; Samjeské, G.; Osawa, M. Formic Acid Electrooxidation on Pd in Acidic Solutions Studied by Surface-Enhanced Infrared Absorption Spectroscopy. *Phys. Chem. Chem. Phys.* **2008**, *10*, 3662–3669.
110. Zhou, Y.; Du, C.; Han, G.; Gao, Y.; Yin, G. Ultra-Low Pt Decorated PdFe Alloy Nanoparticles for Formic Acid Electro-Oxidation. *Electrochim. Acta* **2016**, *217*, 203–209.
111. Wang, J.-Y.; Kang, Y.-Y.; Yang, H.; Cai, W.-B. Boron-Doped Palladium Nanoparticles on Carbon Black as a Superior Catalyst for Formic Acid Electro-Oxidation. *J. Phys. Chem. C* **2009**, *113*, 8366–8372.
112. Xu, H.; Yan, B.; Zhang, K.; Wang, C.; Zhong, J.; Li, S.; Yang, P.; Du, Y. Facile Synthesis of Pd–Ru–P Ternary Nanoparticle Networks with Enhanced Electrocatalytic Performance for Methanol Oxidation. *Int. J. Hydrogen Energy* **2017**, *42*, 11229–11238.
113. Lv, H.; Xu, D.; Sun, L.; Henzie, J.; Suib, S.L.; Yamauchi, Y.; Liu, B. Ternary Palladium-Boron-Phosphorus Alloy Mesoporous Nanospheres for Highly Efficient Electrocatalysis. *ACS Nano* **2019**, *13*, 12052–12061.
114. Scofield, M.E.; Koenigsmann, C.; Wang, L.; Liu, H.; Wong, S.S. Tailoring the Composition of Ultrathin, Ternary Alloy PtRuFe Nanowires for the Methanol Oxidation Reaction and Formic Acid Oxidation Reaction. *Energy Environ. Sci.* **2015**, *8*, 350–363.
115. Vidal-Iglesias, F.J.; Solla-Gullón, J.; Herrero, E.; Aldaz, A.; Feliu, J.M. Pd Adatom Decorated (100) Preferentially Oriented Pt Nanoparticles for Formic Acid Electrooxidation. *Angew. Chem. Int. Ed.* **2010**, *49*, 6998–7001.
116. Yang, F.-K.; Fang, Y.; Li, F.-F.; Qu, W.-L.; Deng, C. Sn-Doped PdCu Alloy Nanosheet Assemblies as an Efficient Electrocatalyst for Formic Acid Oxidation. *Dalt. Trans.* **2023**, *52*, 14428–14434.
117. Lin, X.; Geng, S.; Du, X.; Wang, F.; Zhang, X.; Xiao, F.; Xiao, Z.; Wang, Y.; Cheng, J.; Zheng, Z.; et al. Efficient Direct Formic Acid Electrocatalysis Enabled by Rare Earth-Doped Platinum-Tellurium Heterostructures. *Nat. Commun.* **2025**, *16*, 147.
118. Vidal-Iglesias, F.J.; López-Cudero, A.; Solla-Gullón, J.; Feliu, J.M. Towards More Active and Stable Electrocatalysts for Formic Acid Electrooxidation: Antimony-Decorated Octahedral Platinum Nanoparticles. *Angew. Chem. Int. Ed.* **2013**, *52*, 964–967.
119. Serov, A.; Kwak, C. Recent Achievements in Direct Ethylene Glycol Fuel Cells (DEGFC). *Appl. Catal. B Environ.* **2010**, *97*, 1–12.
120. Gao, J.; Mao, M.; Li, P.; Liu, R.; Song, H.; Sun, K.; Zhang, S. Segmentation and Re-Encapsulation of Porous PtCu Nanoparticles by Generated Carbon Shell for Enhanced Ethylene Glycol Oxidation and Oxygen-Reduction Reaction. *ACS Appl. Mater. Interfaces* **2020**, *12*, 6298–6308.
121. An, L.; Chen, R. Recent Progress in Alkaline Direct Ethylene Glycol Fuel Cells for Sustainable Energy Production. *J. Power Sources* **2016**, *329*, 484–501.
122. Chang, S.C.; Ho, Y.; Weaver, M.J. Applications of Real-Time FTIR Spectroscopy to the Elucidation of Complex Electroorganic Pathways: Electrooxidation of Ethylene Glycol on Gold, Platinum, and Nickel in Alkaline Solution. *J. Am. Chem. Soc.* **1991**, *113*, 9506–9513.
123. Schnaidt, J.; Heinen, M.; Jusys, Z.; Behm, R.J. Electro-Oxidation of Ethylene Glycol on a Pt-Film Electrode Studied by Combined in Situ Infrared Spectroscopy and Online Mass Spectrometry. *J. Phys. Chem. C* **2012**, *116*, 2872–2883.
124. Wang, Y.; Zhuo, H.; Sun, H.; Zhang, X.; Dai, X.; Luan, C.; Qin, C.; Zhao, H.; Li, J.; Wang, M. Implanting Mo Atoms into Surface Lattice of Pt_3Mn Alloys Enclosed by High-Indexed Facets: Promoting Highly Active Sites for Ethylene Glycol Oxidation. *ACS Catal.* **2018**, *9*, 442–455.
125. Bai, S.; Wang, C.; Deng, M.; Gong, M.; Bai, Y.; Jiang, J.; Xiong, Y. Surface Polarization Matters: Enhancing the Hydrogen-evolution Reaction by Shrinking Pt Shells in Pt–Pd–Graphene Stack Structures. *Angew. Chem. Int. Ed.* **2014**, *53*, 12120–12124.
126. Li, C.; Yuan, Q.; Ni, B.; He, T.; Zhang, S.; Long, Y.; Gu, L.; Wang, X. Dendritic Defect-Rich Palladium–Copper–Cobalt Nanoalloys as Robust Multifunctional Non-Platinum Electrocatalysts for Fuel Cells. *Nat. Commun.* **2018**, *9*, 3702.
127. Robinson, A.M.; Mark, L.; Rasmussen, M.J.; Hensley, J.E.; Medlin, J.W. Surface Chemistry of Aromatic Reactants on Pt-and Mo-Modified Pt Catalysts. *J. Phys. Chem. C* **2016**, *120*, 26824–26833.

128. Demarconnay, L.; Brimaud, S.; Coutanceau, C.; Léger, J.-M. Ethylene Glycol Electrooxidation in Alkaline Medium at Multi-Metallic Pt Based Catalysts. *J. Electroanal. Chem.* **2007**, *601*, 169–180.
129. Yang, Y.-Y.; Ren, J.; Zhang, H.-X.; Zhou, Z.-Y.; Sun, S.-G.; Cai, W.-B. Infrared Spectroelectrochemical Study of Dissociation and Oxidation of Methanol at a Palladium Electrode in Alkaline Solution. *Langmuir* **2013**, *29*, 1709–1716.
130. Hahn, F.; Beden, B.; Kadirgan, F.; Lamy, C. Electrocatalytic Oxidation of Ethylene Glycol: Part III. In-Situ Infrared Reflectance Spectroscopic Study of the Strongly Bound Species Resulting from Its Chemisorption at a Platinum Electrode in Aqueous Medium. *J. Electroanal. Chem. Interfacial Electrochem.* **1987**, *216*, 169–180.
131. Leung, L.W.H.; Weaver, M.J. Real-Time FTIR Spectroscopy as a Quantitative Kinetic Probe of Competing Electrooxidation Pathways of Small Organic Molecules. *J. Phys. Chem.* **1988**, *92*, 4019–4022.
132. Christensen, P.A.; Hamnett, A. The Oxidation of Ethylene Glycol at a Platinum Electrode in Acid and Base: An in Situ FTIR Study. *J. Electroanal. Chem. Interfacial Electrochem.* **1989**, *260*, 347–359.
133. Wang, H.; Jiang, B.; Zhao, T.-T.; Jiang, K.; Yang, Y.-Y.; Zhang, J.; Xie, Z.; Cai, W.-B. Electrocatalysis of Ethylene Glycol Oxidation on Bare and Bi-Modified Pd Concave Nanocubes in Alkaline Solution: An Interfacial Infrared Spectroscopic Investigation. *ACS Catal.* **2017**, *7*, 2033–2041.
134. Wang, P.; Lin, X.; Yang, B.; Jin, J.-M.; Hardacre, C.; Yu, N.-F.; Sun, S.-G.; Lin, W.-F. Activity Enhancement of Tetrahexahedral Pd Nanocrystals by Bi Decoration towards Ethanol Electrooxidation in Alkaline Media. *Electrochim. Acta* **2015**, *162*, 290–299.
135. Bambagioni, V.; Bevilacqua, M.; Bianchini, C.; Filippi, J.; Marchionni, A.; Vizza, F.; Wang, L.Q.; Shen, P.K. Ethylene Glycol Electrooxidation on Smooth and Nanostructured Pd Electrodes in Alkaline Media. *Fuel Cells* **2010**, *10*, 582–590.
136. Cheng, J.; Tu, Y.; Xiang, Y.; Ni, J.; Guo, T.; Huang, X.; Liu, B.; Wei, Z. Anti-Poisoning of CO and Carbonyl Species over Pd Catalysts during the Electrooxidation of Ethylene Glycol to Glycolic Acid at Elevated Current Density. *Chem. Sci.* **2025**, *16*, 4303–4310.
137. Wang, C.; Xu, H.; Shang, H.; Jin, L.; Chen, C.; Wang, Y.; Yuan, M.; Du, Y. Ir-Doped Pd Nanosheet Assemblies as Bifunctional Electrocatalysts for Advanced Hydrogen Evolution Reaction and Liquid Fuel Electrocatalysis. *Inorg. Chem.* **2020**, *59*, 3321–3329.
138. Wang, Y.; Zheng, M.; Sun, H.; Zhang, X.; Luan, C.; Li, Y.; Zhao, L.; Zhao, H.; Dai, X.; Ye, J.-Y.; et al. Catalytic Ru Containing Pt3Mn Nanocrystals Enclosed with High-Indexed Facets: Surface Alloyed Ru Makes Pt More Active than Ru Particles for Ethylene Glycol Oxidation. *Appl. Catal. B Environ.* **2019**, *253*, 11–20.
139. Qin, Y.; Zhang, W.; Wang, F.; Li, J.; Ye, J.; Sheng, X.; Li, C.; Liang, X.; Liu, P.; Wang, X. Extraordinary p–d Hybridization Interaction in Heterostructural Pd-PdSe Nanosheets Boosts C–C Bond Cleavage of Ethylene Glycol Electrooxidation. *Angew. Chem. Int. Ed.* **2022**, *61*, e202200899.
140. Yang, X.; Yao, K.X.; Ye, J.Y.; Yuan, Q.; Zhao, F.; Li, Y.; Zhou, Z. Interface-Rich Three-Dimensional Au-Doped PtBi Intermetallics as Highly Effective Anode Catalysts for Application in Alkaline Ethylene Glycol Fuel Cells. *Adv. Funct. Mater.* **2021**, *31*, 2103671.